University of Coimbra

Master's Degree in Biomedical Engineering

# Fat Quantification in Liver using Chemical Shift Imaging

*Author*

Mário J. P. Ribeiro

*Supervisor*

Sónia I. Gonçalves

*A thesis submitted in fulfilment of the requirements*

*for the Master's Degree in Biomedical Engineering*

*in the*

Faculty of Sciences and Technology


October 2013

UNIVERSITY OF COIMBRA

# *Abstract*

Faculty of Science and Technology

Department of Physics

Master's Degree in Biomedical Engineering

**Fat Quantification in Liver using Chemical Shift Imaging**

by Mário J. P. Ribeiro

MRI is becoming increasingly important in the characterization of NAFLD, which is one of the most relevant diffuse liver diseases with increasing prevalence in the developed countries. Currently, biopsy is the gold standard in the early identification and staging of NAFLD, which is crucial to evaluate the risk of hepatocellular carcinoma development. However, the later is associated with sampling errors and with the development of several post-surgical complications. In this work, we address the problem of quantifying the fat accumulation in the liver using a non-invasive procedure based on chemical shift imaging and two signal models, the magnitude and complex models. In particular, we address the influence of noise, relaxation effects and choice of echo times in fat fraction estimation error. Our approach relied in the development of a new acquisition strategy based on the optimal choice of echo times, which were evaluated in simulation studies and later tested with phantoms. A program to perform *in-vivo* fat quantification was implemented, extending our approach to clinical data. Results indicate that good fat fraction estimation can be achieved by correctly choosing the echo times. However, it is extremely difficult to find a single echo time combination which optimize a large range of fat fractions. Finally, we also demonstrate that the standard clinical protocol has several flaws and that a new acquisition protocol must be developed.

# *Acknowledgements*

I would like to express my appreciation to all those who provided me the possibility to complete this project at the the Instítuto de Ciências Nucleares Aplicadas a Saúde (ICNAS). A special gratitude I give to my supervisor, Professor Sónia I. Gonçalves, whose contribution, support, comments and guidance helped me to achieve the project goals and improve several skills.

Furthermore, I would like to acknowledge with much appreciation the crucial role of José Sereno, PhD student during the construction of the phantom used in the project. A special thanks goes to the staff of the Association Apojovi/Aposenior for all the support and understanding in the several times I had to skip work in order to continue this project.

Many thanks go to all my friends particularly João Martins, Jorge Morais, Luís Antunes, Ricardo Rosado and Vanessa Marques for all the support; your friendship and advises were fundamental to overcome the many challenges during this year. Last but not the least, my gratitude also goes to Leandro Silva, Marina Bragança and Vitor Bragança, my long-time friends.

# Contents

# List of Figures

# List of Tables

# Abbreviations

| | |
|---|---|
| **ADC** | **A**nalog-to-**D**igital **C**onversion |
| **FF** | **F**at **F**raction |
| **FOV** | **F**ield **O**f **V**iew |
| **GRE** | **GR**adient-**E**cho |
| **Gpe** | **G**radient **p**hase **e**ncoding |
| **Gro** | **G**radient **R**ead**o**ut |
| **Gss** | **G**radient **S**lice **S**election |
| **HCC** | **H**epatocellular **C**arcinoma |
| **ME** | **M**ulti **E**choe |
| **MR** | **M**agnetic **R**esonance |
| **MRI** | **M**agnetic **R**esonance **I**maging |
| **MRS** | **M**agnetic **R**esonance **S**pectroscopy |
| **NA** | **N**oise **A**mplitude |
| **NAFLD** | **N**on **A**lcoholic **F**atty **L**iver **D**isease |
| **NASH** | **N**on **A**lcoholic **S**eato**H**epatitis |
| **NSA** | **N**umber of **S**ignal **A**averages |
| **RF** | **R**adio**F**requency |
| **RNA** | **R**relative **N**oise **A**mplitude |
| **ROI** | **R**region **O**f **I**nterest |
| **SDS** | **S**odium **D**odecyl **S**ulphate |
| **SE** | **S**pin-**E**cho |

# Symbols

| | |
|---|---|
| $\alpha$ | Flip Angle |
| $B_0$ | External Magnetic Field |
| $B_1$ | Radiofrequency |
| $\vec{M}$ | Net Magnetization |
| $\vec{M}_x$ | Net Magnetization component along x-axis |
| $\vec{M}_y$ | Net Magnetization component along y-axis |
| $\vec{M}_z$ | Net Magnetization component along z-axis |
| $S$ | Signal Intensity |
| $S_f$ | Fat Signal Intensity |
| $S_w$ | Water Signal Intensity |
| $T_1$ | Spin-Lattice Relaxation |
| $T_2$ | Spin-Spin Relaxation |
| $T'_2$ | Relaxation Time due to $B_0$ inhomogeneities |
| $T_2^*$ | Total Transverse Relaxation time |
| $TE$ | Echo Time |
| $TR$ | Repetition Time |
| $\omega_0$ | Larmor Frequency |
| $\omega_1$ | Spin Frequency due to $B_1$ |
| $\gamma$ | Gyromagnetic Ratio |
| $\sigma$ | Chemical Shift Term |
| $\phi$ | Phase Accumulation due to $B_0$ Inhomogeneities |

*To my parents. . .*

# Chapter 1

# Introduction

## 1.1 Motivation and objectives

The western life style keeps on changing: obesity and problems that emerge from fat accumulation are a well-known issue nowadays. Public and private health institutions, governmental associations and even the media have been promoting awareness campaigns aiming to minimize and prevent what can be seen as a public health problem. An increasing topic of interest is, therefore, fat accumulation in the liver, which gives rise to Non Alcoholic Fatty Liver Disease (NAFLD). NAFLD is a diffuse liver disease which is not related to alcohol consumption, but rather linked to the metabolic syndrome [1]. It comprises a spectrum of clinical conditions of increasing severity that range from simple steatosis to non-alcoholic steato-hepatitis (NASH), fibrosis, and finally cirrhosis [1, 2].

The characterization and staging of NAFLD is increasingly important since several studies recognize NAFLD as the most common cause of chronic liver disease with a high prevalence worldwide, particularly in the western world. Currently, liver biopsy is the gold standard in early assessment of NAFLD. However, the latter is an invasive and expensive method prone to sampling errors and low accuracy [1–3].

With the evolution of technology and the increased interest on biomedicine, magnetic resonance (MR) chemical shift methods appeared as non-invasive alternative to biopsy in the early characterization and staging of NAFLD. The

idea was simple but very effective; take advantage of the difference in the resonance frequency between the protons of water and fat, a property known as chemical shift, to quantify the amount of fat present in the liver [4]. MR spectroscopy (MRS), which takes advantage of the chemical shift effect to detect and quantify various chemical species, led to several advances in quantitative fat estimation and it is now considered the safest and most accurate non-invasive method. However, MRS is performed on a single-voxel basis, thus introducing variability at the same time that is time consuming and therefore not suitable for normal clinical routine [5, 6]. In contrast, chemical shift imaging emerges as an attractive method for fat quantification on a voxel-by-voxel basis since it allows for whole-liver coverage, it is widely accessible and easy to use. In fact, it is well established in the literature that if the signals from water and fat protons were correctly separated, accurate fat quantification would be possible [4–6]. Nevertheless, the correct mathematical modulation of the signal, the noise, the relaxation effects as well as the errors introduced by external magnetic field inhomogeneities are confounding factors in fat quantification, introducing errors in the estimates [4, 7].

Although, many advances were made regarding fat quantification with chemical shift imaging, there are still many methodological questions that remain open. Particularly, the properly evaluation and addressing of the echo times, that are used to sample de data during the several scans that are acquired at multiple echo times.

The present work, which aims to optimize fat quantification in the liver using chemical shift imaging, consists of three main parts: the first one is a simulation study where the accuracy of several signal models are tested with respect to liver fat fraction quantification at 3T, In particular, the influence on fat fraction bias and error of sampling the signal with different echo times combinations, will be explored. The second part consists in identifying the echo time combinations that minimize both fat fraction bias and error. Subsequently, appropriate phantoms will be built in order to test experimentally the results obtained in the simulation study. Finally, the third part of this work consists in developing a software to produce parametric maps of liver fat fraction based on clinical data.

## 1.2 Theoretical background

### 1.2.1 The liver: a brief overview

The liver (figure 1.1) is the largest internal organ weighting approximately 1.3Kg to 1.7Kg. It is located in the upper right quadrant of the abdominal cavity under the right hemidiaphragm; lying to the right of the stomach and overlying the gallbladder [8, 9]. At the anatomic level, four lobes can be identified: the left, right, caudate and quadrate lobes [9]. The lobes are than divided in lobules which are the functional units of the liver, containing the hepatic cells [8, 10]. The liver is also connected to two major afferent blood vessels, the hepatic artery and the portal vein, by which it gets its blood supplies. These vessels branch themselves into minor vessels, forming the capillary network, which reaches the lobules and intervene in the liver functions [8, 9].

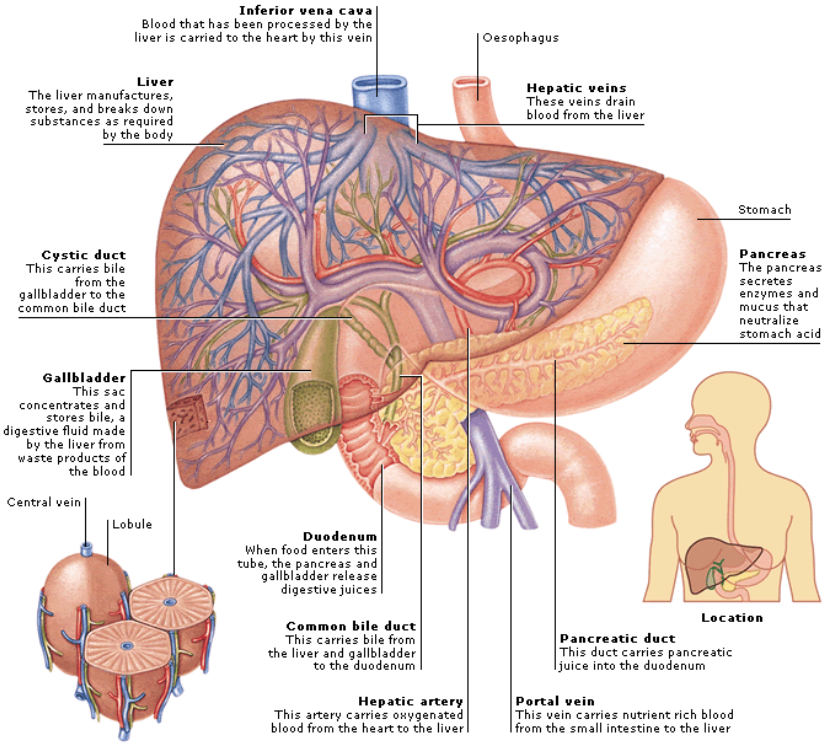


FIGURE 1.1: The Liver: general anatomy and location. Source: aviva.com.uk, medical encyclopaedia

The epithelial cell population consists of the hepatocytes (parenchymal cells) and the cholangiocytes, which are the two main cell types in the lobules. The hepatocytes correspond to approximately 80% of the livers volume and are the key effectors in its activity [10]. However, this convention is somewhat wrong.

In fact, together with the hepatocytes, several other cells work as an integrated community to carry-out the liver functions. This functional integration is obtained by several communication mechanisms, such as signalling networks [10].

As far as physiological functions are concerned, the liver has a well-established role in several functions:

1) **Digestion:** Due to its secretory function, the liver can be considered a gland. The hepatocytes produce and excrete the bile, a fluid that is storaged in the gallbladder and delivered into the small intestine. The bile aides in the digestion of fat and in the absorption of fat soluble nutrients [10, 11].

2) **Metabolism:** The liver is involved in several metabolic processes. For example, it regulates the levels of glucose in the blood flow as well as the storage of fat. The production, metabolism and excretion of cholesterol is also controlled by the liver [10, 11].

3) **Storage:** The liver stores several nutrients such as vitamins A, B-9 and D. Furthermore it also stores iron, which can be used to form heme groups, such as the ones present in hemoglobin [10, 11].

4) **Detoxification:** The liver plays a major role in helping the organism metabolizing toxic substances that have been absorbed. Substances like alcohol, drugs, pesticides, and heavy metals which are absorbed in the digestion are delivered into the liver through the portal vein. The liver filters and processes these substances, and excretes them to the bile. Normal bio products of the metabolism are also metabolized by the liver [10].

5) **Protein synthesis:** The liver is involved in the synthesis of several proteins, including enzymes and hormones [10, 11].

### 1.2.2 Non Alcoholic Fatty Liver Diseases

Normal liver activity can be affected by several factors which can lead to severe health issues.NAFLD is an heterogeneous liver pathology that is not linked to

alcohol consumption, but rather to the metabolic syndrome [1]. NAFLD comprises a vast spectrum of pathologies of increasing severity and that range from fat accumulation inside the hepatocytes (steatosis) to non-alcoholic steatohepatitis (NASH), that lead to fibrosis and cirrhosis (figure 1.2) [1–3, 12].

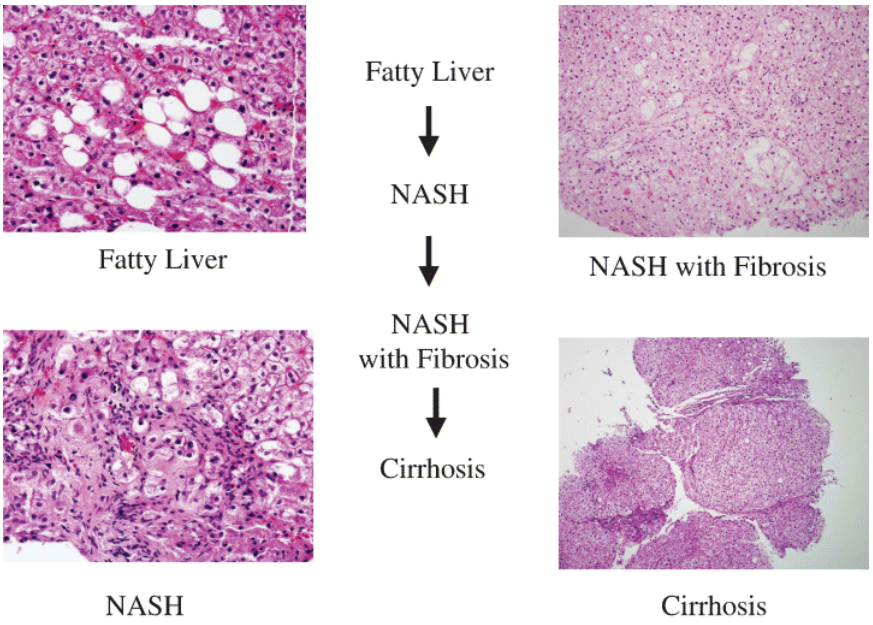


FIGURE 1.2: Stages of NAFLD and corresponding histological appearance. Adapted from [13].

The first stage of NAFLD is the simple accumulation of fat droplets within the hepatocytes, a condition known as steatosis [3, 12]. In order for a subject to be classified as having steatosis, fat accumulation in the liver must exceed 5% to 10% by weight [1, 2]. Steatosis in itself is not associated with increased short-term morbidity nor mortality. However, it can trigger the progression to more severe stages of NAFLD such as NASH [2, 12, 14]. The mechanisms by which this triggering takes place are still largely unknown, but it is believed that fat accumulation increases the probability of cell injury [1].

NASH is characterized by excessive fat accumulation combined with liver cell injury, inflammation and necrotic activity [1, 2, 14]. It is correlated both with morbidity and mortality, and it is increasingly becoming a reason for liver transplantation [14]. In addition, NASH dramatically increases the risk of fibrosis, cirrhosis, liver failure and hepatocellular carcinoma (HCC) [1, 12]. In the last two stages of NAFLD, there is the replacement of liver tissue by fibrotic tissue, with the loss of lobular architecture and severe cell injury. At these stages, patients are at a higher risk of developing HCC [2].

#### 1.2.2.1 Pathogenesis

The exact pathogenesis of NAFLD remains poorly understood. However, it is widely considered to be the manifestation of the metabolic syndrome, i.e. related to Diabetes Mellitus Type 2, insulin resistance and obesity [1, 14].

The most widely accepted explanation for NAFLD pathogenesis is the multi-hit hypothesis. In this hypothesis, multiple hits are in the origin of the disease and its progression, with the metabolic syndrome playing a central role [14]. Insulin resistance is associated with fat retention, which makes it closely related to obesity, and is considered to play a major role in NAFLD pathogenesis [2, 14, 15].

#### 1.2.2.2 Epidemiology

Recent studies recognize NAFLD as the most common cause of chronic liver diseases [1, 14, 16, 17]. Although, geographic variations in its prevalence are notorious, NAFLD affects all racial and ethnic groups as well as ages and genres [18] and it has been reported worldwide with a distribution that is closely associated with diabetes and obesity [14, 18]. The latter conditions are now reaching epidemic proportions, particularly obesity, and serve as a good overview for the incidence of NAFLD as figure 1.3 shows. Furthermore, NAFLD prevalence is increasing, particularly in the western world [14, 18].

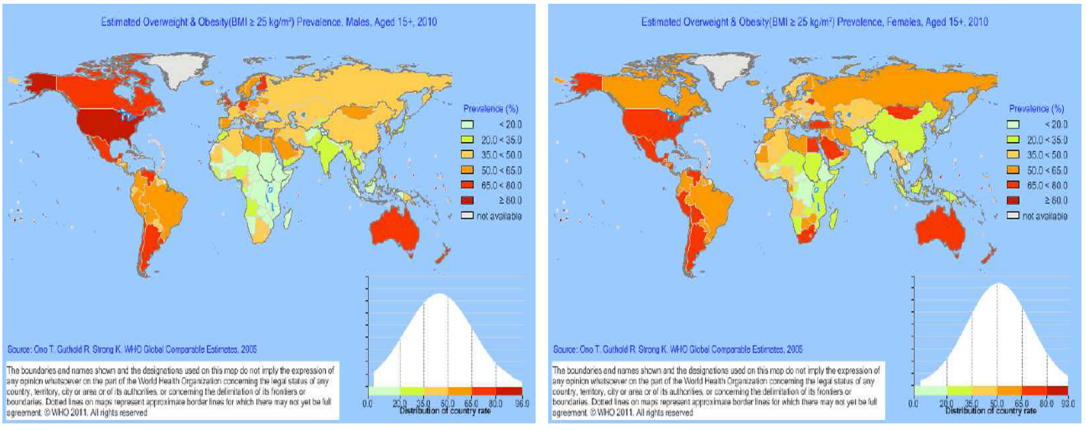


FIGURE 1.3: Estimated worldwide prevalence of obesity in males and females aged above 15 in 2010. Source: WHO [14]

A number of studies indicate that, only in the United States of America, 30% of the general population is affected. The same reports estimate an incidence of

10% to 30% on the world population [16, 17]. The prevalence among children is pointed to be up to 10% overall, being that the incidence in obese children is even more severe and reported to be up to 53% [19]. Although Gastadelli et al, 2007, report that 80% to 90% of the identified cases rely on simple steatosis, Falck-Ytter et al, 2011, showed that up to 20% of patients with steatosis develop NASH and cirrhosis [19, 20]. Moreover, according to new data presented in the International Liver Congress of 2011, the prevalence of NAFLD is expected to increase, in the USA alone, by 50% in 2030, thus reaching epidemic proportions.

#### 1.2.2.3 Diagnosis

As previously shown, the worldwide prevalence of NAFLD is large, which implies that its diagnosis and early assessment are extremely important. As a consequence, several studies using various medical imaging techniques, have been proposed to help in the early diagnosis and assessment of NAFLD.

Ultrasound imaging detects fat accumulation in the liver. However, it cannot quantify fat and subsequently differentiate between stages, therefore it often requires further evaluation with other techniques, such as biopsy [3]. Liver biopsy is currently the gold standard in NAFLD early assessment [1, 2, 12, 14]. However, this technique presents several drawbacks, the most important of which are the high cost, potential post-surgical complications, and inherent sampling bias. The latter is very important for the correct diagnose based on biopsy, since fat infiltrations are heterogeneously distributed while biopsy only samples one or few liver portions. Finally, hepatic biopsy is a highly invasive procedure with risk of morbidity and even mortality: about 1% to 3% of the patients require hospitalization and the complications may vary with the procedure [21].

### 1.2.3 MRI fundamentals

MRI is a medical image technique based on the interaction of nuclear spins (protons in the hydrogen atoms of water molecules) with an external magnetic field, $B_0$ [22–25]. Due to its abundance in the human body, $^1H$ nuclei are typically used in MRI to produce images with various types of contrast [22, 23].

The generation of signal to produce images is based on the manipulation and detection of the magnetization that is available in the sample [22–24].

In the absence of $B_0$, each spin ensemble element (with individual magnetic moment ($\vec{\mu}$) of equal magnitude) is randomly oriented. As a consequence, the resulting net magnetization is zero. In the presence of $B_0$, the magnetic moments tend to align with the direction of $B_0$ in two orientations: parallel and anti-parallel to $B_0$. At room temperature there is small excess of spins aligned parallel to $B_0$ which produce the net equilibrium, $\vec{M}_0$ [22, 23]. Furthermore, the spin precesses around the axis defined by the direction of $B_0$ at a constant (Larmor) frequency [22] which is given by the Larmor equation

$$\omega_0 = \gamma B_0 \tag{1.1}$$

where $\gamma$ is the gyromagnetic ratio.

In the absence of any other magnetic field, the net magnetization ($\vec{M}$) remains at equilibrium, i.e. aligned parallel to the direction of $B_0$, and no signal is generated. In order to produce an MR image, the magnetization has to be excited away from its equilibrium position. This is accomplished by the application of a radiofrequency (RF) pulse ($B_1$) that is applied to the system orthogonally to $B_0$, for a short period [22, 23]. If the sample is irradiated with an RF pulse with frequency ($\omega_{RF} = \omega_0$ (on resonance condition)), the spins absorb the RF energy, thereby causing the net magnetization, $\vec{M}$, to move away from its original equilibrium position and to rotate around an axis perpendicular to both $B_0$ and $B_1$ (figure 1.4) [22]. Following RF excitation, $\vec{M}$ will have a longitudinal component $\vec{M}_z$, parallel to $B_0$, and a transverse component $\vec{M}_t$, perpendicular to $B0$, which will continue precessing around $B_0$ at the Larmor frequency [22, 23]. The variation in $\vec{M}_t$ generates an RF signal which is detected with a coil by magnetic induction and that is used for image reconstruction [22–25].

#### 1.2.3.1 Relaxation effects and Bloch equation

**Relaxation effects**

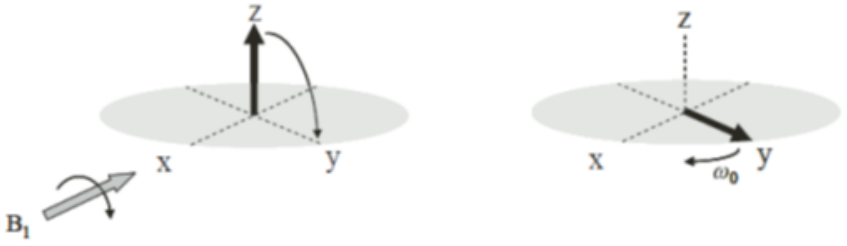


FIGURE 1.4: The application of an RF pulse, $B_1$, along the direction of x causes $\vec{M}$ to rotate in the direction of y (Left). Precession movement in the xy plane (right) [25].

After excitation, and in the absence of any other RF pulse, the spins release the absorbed energy and $\vec{M}$ returns progressively to equilibrium. This process is called relaxation and it is governed by two time constants: $T_1$ and $T_2$ [22–25].

During $T_1$ relaxation or spin-lattice relaxation, the spins release their energy to the surrounding atomic lattice. As a consequence, $\vec{M}_z$ returns progressively to its equilibrium value. The rate at which spin-lattice relaxation takes place is controlled by the $T_1$ relaxation time constant. Generally, $T_1$ times are in the order of several hundreds of milliseconds and vary from tissue to tissue as well as with the intensity of $B_0$ [23–25]. The $T_2$ relaxation time, also called spin-spin relaxation, is associated with the transverse decay of $\vec{M}$ [22, 23]. Spins experience local fields produced by the surrounding protons. This leads to different local precessional frequencies and subsequently to the loss of phase coherence or dephasing, as figure 1.5 illustrates. Dephasing decreases transverse magnetization and reduces signal intensity [22, 23].

The presence of spatially varying inhomogeneities in $B_0$ are also responsible for the dephasing of transverse magnetization. This type of relaxation is controlled by the $T_2'$ relaxation time constant [22, 25]. Thus, the total transverse relaxation is the summed effect of spin-spin interaction and magnetic field inhomogeneities, and it is characterized by the $T_2^*$ relaxation time constant, defined as

$$\frac{1}{T_2^*} = \frac{1}{T_2'} + \frac{1}{T_2} \tag{1.2}$$

The values of $T_2$ and $T_2^*$, which are in the order of the milliseconds, vary from tissue to tissue and are dependent of the strength of the applied $B_0$; overall, $T_1 > T_2 > T_2^*$ [22].

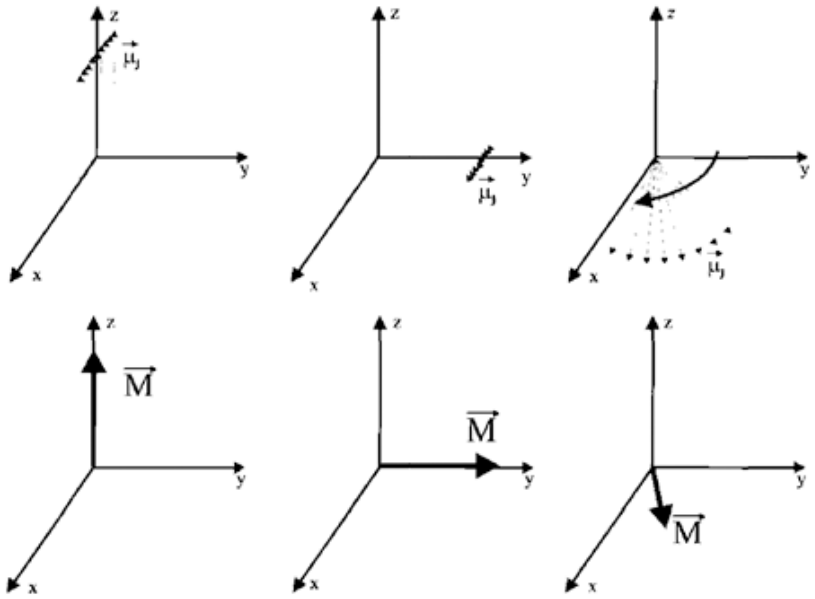


FIGURE 1.5: Dephasing of spins in the transverse plane due to $T_2$ relaxation (above) and its influence on the net magnetization intensity (below)[22].

### Bloch Equations in the absence of $B_1$

The Bloch equations [22] describe the magnetization in presence of $B_0$, $B_1$ and relaxation effects as

$$\frac{dM_z}{dt} = -\omega_1 M_y + \frac{M_0 - M_z}{T_1} \tag{1.3}$$

$$\frac{dM_x}{dt} = \Delta\omega M_y - \frac{M_x}{T_2} \tag{1.4}$$

$$\frac{dM_y}{dt} = -\Delta\omega M_x + \omega_1 M_z - \frac{M_y}{T_2} \tag{1.5}$$

where $M_0$ is the value of the equilibrium magnetization, $\omega_1$ is the spin frequency due to the RF field and $M_z$ , $M_x$ and $M_y$ are the magnetization components along x-, y-, and z-axis respectively. $\Delta\omega$ represents the difference between $\omega_0$ and $\omega$, where $\omega$ is the RF pulse frequency. It is furthermore assumed, without loss of generality, that $B_0$ is oriented along the z-axis and that $M_z$ and $M_x(M_y)$ are the longitudinal and transverse components of $\vec{M}$ respectively. $B_1$ is also considered to be much smaller than $B_0$ [22].

When only $B_0$ and relaxations effects are considered, equations 1.3, 1.4 and 1.5 are written as

$$\frac{dM_z}{dt} = \frac{M_0 - M_z}{T_1} \tag{1.6}$$

$$\frac{dM_x}{dt} = \omega_0 M_y - \frac{M_x}{T_2} \tag{1.7}$$

$$\frac{dM_y}{dt} = -\omega_0 M - \frac{M_y}{T_2} \tag{1.8}$$

Solving for 1.6, the following solution is obtained:

$$M_z(t) = M_z(0)e^{-t/T_1} + M_0(1 - e^{-t/T1}) \tag{1.9}$$

This expression quantifies $T_1$ relaxation, i.e. it shows the evolution from the initial magnetization value after excitation, $M_z(0)$, to the equilibrium value $M_0$ [22]. The solution to 1.7 and 1.8 is

$$M_x(t) = e^{-t/T_2}(M_x(0)cos\omega_0 t + M_y(0)sin\omega_0 t) \tag{1.10}$$

$$M_y(t) = e^{-t/T_2}(M_y(0)cos\omega_0 t - M_x(0)sin\omega_0 t) \tag{1.11}$$

Which corresponds to the $T_2$ exponential decay of the transverse magnetization that is precessing around $B_0$ (z-axis) with an angular frequency $\omega_0$ [22].

#### 1.2.3.2 Spatial encoding

The goal of MRI is the spatial localization of MR signals in order to be able to reconstruct an image. Spatial encoding of the MR signal in three dimensions is obtained by applying magnetic field gradients in three different directions. These gradients produce a signal with spatially varying frequency components in accordance with

$$\omega(x) = \gamma B(x) \tag{1.12}$$

Where x is the spatial coordinate along the direction of the gradient and $B(x)$ is the magnetic field that spins, at position x along the gradient direction, experience [22].

Three main gradients are used to perform spatial encoding: Slice selection (Gss); Phase encoding (Gpe) and Readout or Frequency encoding gradient (Gro) [23–25].

The first step in spatial encoding is the selection of a slice plane to be imaged. Two main components are involved in this process: the selective RF pulse and Gss. The selective RF pulse has a limited bandwidth of frequencies which are related to slice thickness. When this pulse is applied in the presence of Gss, a portion of the sample, coincident with the desired slice location and thickness, is excited [23, 24]. During phase encoding, Gpe induces a constant spin dephasing along the direction of Gpe. As a consequence, spins at different positions along that direction will precess at the same frequency but with different phases. Thus, phase encoding locates the MR signal along Gpe direction through spin phase variation [23, 24]. Finally, the effect of Gro is to cause a variation of the spin precession frequency along its direction. This frequency variation encodes the third spatial coordinate and allows for image reconstruction using Fourier Transformation [23–25].

#### 1.2.3.3 Pulse sequences

Pulse sequences are the methodology by which an MRI image is acquired, and involve the manipulation of e.g. RF pulses, gradients analog-to-digital conversion (ADC), which are usually applied with a fixed pre-determined order – pulse sequences [23]. Several parameters are important in pulse sequences, namely the repetition time (TR), the echo time (TE) and flip angle ($\alpha$). The TR corresponds to the time between successive excitation RF pulses whereas $\alpha$ is the angle by which the magnetization is tipped away relative to the $B_0$ direction by the application of the RF pulse. Finally, TE is defined as the time from the excitation pulse to the time point where maximum signal is detected [23].

There are two main families of pulse sequences: Spin-echo (SE) and Gradient-echo (GRE) sequences [22, 23].

Spin-echo sequences are the most commonly used in clinical procedures. This technique is characterized by the use of, at least, two RF pulse: an RF excitation pulse, generally with a flip angle of $90^o$, and one (or more) $180^o$ refocusing pulse, which is applied to rephase the signal and to generate a spin-echo. If more than a spin-echo is desired, then several $180^o$ refocusing pulses are necessary [23].

The second type of pulse sequences are the gradient-echo sequences. In contrast to spin-echo sequences, these sequences do not use RF refocusing pulses. Gradient reversal is used instead for magnetization rephasing and signal generation the gradient-echoes. Another difference with respect to SE sequences is that flip angles lower than $90^o$ are generally used. Furthermore, GRE sequences are typically weighted on $T_2^*$ [22, 23]. In this work, the pulse sequence that is used for data acquisition is of the GRE type.

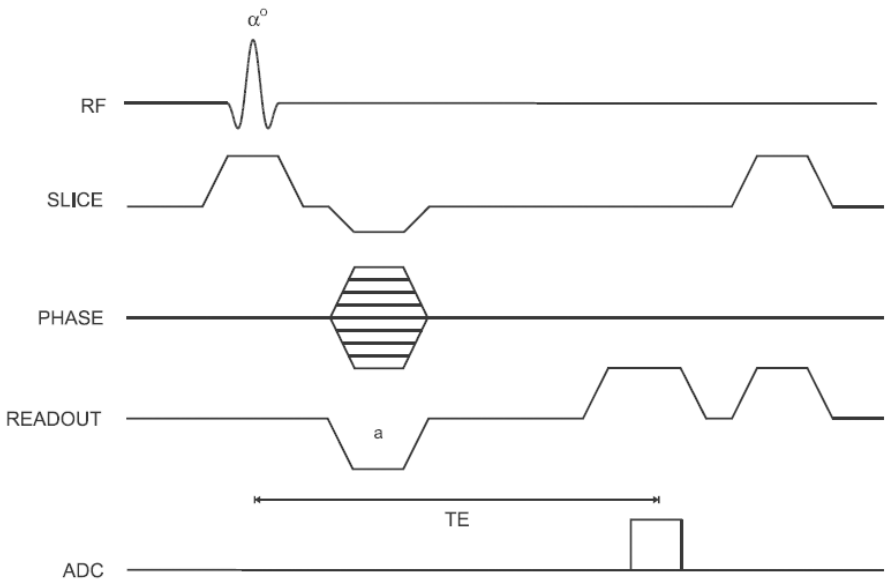


FIGURE 1.6: Spoiled GRE sequence timing diagram, 2D method. Because there is no $180^o$ RF pulse, the polarity of Gro dephasing gradient pulse (a) is opposite that of the readout gradient pulse applied during signal detection. The TE is measure from the middle of the excitation to the center of the echo [25].

#### 1.2.3.4 Chemical shift imaging

The precession frequency of spins depends on the local magnetic field that each individual spin experiences. So far, it was assumed that only $B_0$ contributes to this local magnetic field. However, in reality each spin has its own local

magnetic field, which is determined by which molecules and atoms exist in the neighbourhood of the spin [22, 23, 25].

In MRI, the signal comes essentially from the protons in water molecules and in the chains of fatty acids [22, 23, 25]. Protons from water and fatty acids experience different chemical environments and have distinct electron configurations, as figure 1.7 shows [25].

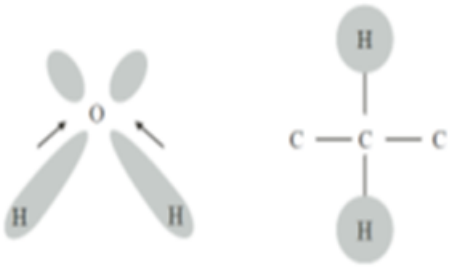


FIGURE 1.7: Chemical environment of water (left) and fat protons with the shading regions illustrating the electron density distribution [25].

Because of its molecular environment, the water proton experiences a local magnetic field which is different from that of a fat proton. This local difference is known as chemical shielding and leads to slightly different Larmor frequencies, for water and fat [22, 23, 25]. Such frequencies can be described in terms of chemical shifts, $\sigma$, which is defined as

$$B_{shifted}(j) = (1 - \sigma_j)B_0 \tag{1.13}$$

Where $B_{shifted}$ is the the local magnetic field difference and $j$ represents the chemical compound, which in the present work is fat. The chemical shift term is generally small and it is expressed in parts-per-million (ppm) with a value of 3.5 for fat (figure 1.8) [22, 23]. The difference in the Larmor frequency from fat relative to water depends also on $B_0$ and is given by

$$\Delta\omega_0 = \gamma\sigma B_0 \tag{1.14}$$

where for $B_0 = 3T$ the chemical effect is approximately equal to 450Hz [23].

This difference in frequencies causes the fat protons to precess slower than the water protons. As a consequence, the water and fat magnetization components

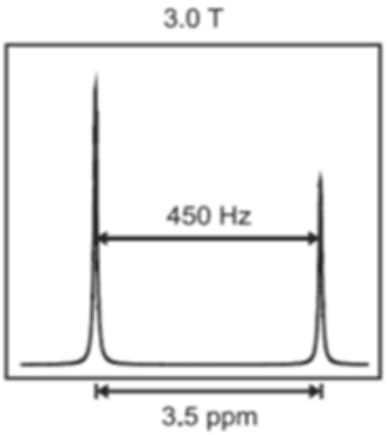


FIGURE 1.8: Spectrum of water and fat at 3T. The resonance frequencies are separated by 3.5ppm which corresponds to a frequency difference of 450HZ [23].

are in phase and out of phase (oppose-phase), depending of the TEs, as illustrate in figure 1.9 [22, 23].

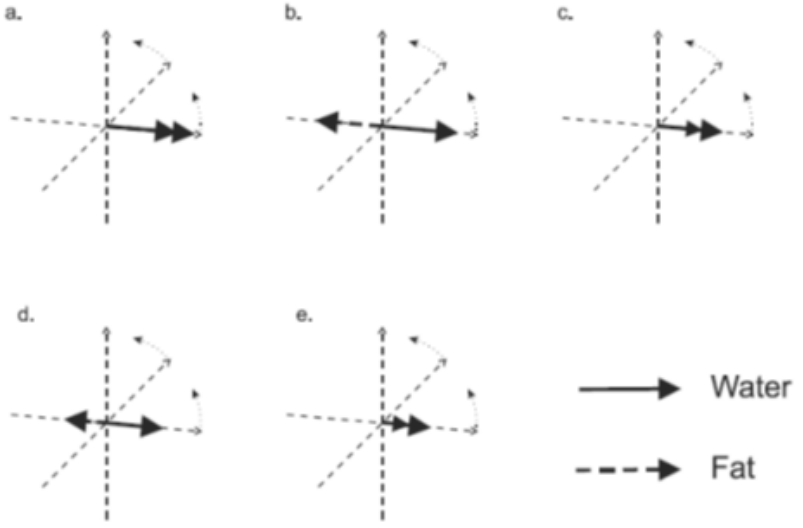


FIGURE 1.9: Precession of fat and water protons. Due to the difference in the resonance frequencies, the two components are in phase (a, c and e) and out of phase (b and d) at distinct TEs [23].

In the SE sequences, the chemical shift effect is compensated by the $180^o$ RF refocusing pulse which implies that water and fat protons are always in-phase. In GRE sequences there is no compensation and therefore both chemical species acquire phase with respect to each other that is proportional to TE. In a voxel containing water and fat, when both components are in-phase, a reinforcement of the signal is observed. when both components are out-of-phase there is signal cancelation as illustrated in figure 1.10 [22, 23].

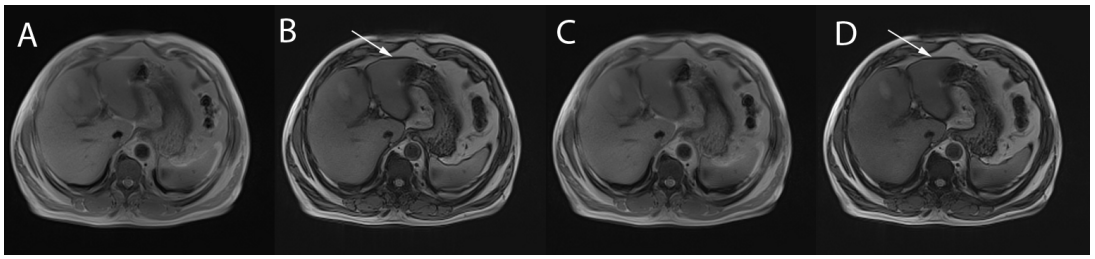


FIGURE 1.10: In-phase (A and C) and opposed-phase (B and D) abdominal images acquired using a GRE sequence. Arrows indicating the phase cancelation in voxels containing water and fat.

Chemical shift imaging takes advantage of the abovementioned properties and it is referred as the process by which identical nuclei, experiencing different levels of shielding, are selectively imaged [22].

### 1.2.4 NAFLD and chemical shift imaging

Since Dixon (1984) first proposed the two-points Dixon technique to decompose the water and fat components based on two images (in-phase and opposed-phase) [26], many advances on chemical shift imaging for fat quantification were made. Two main models have been used to separate water and fat components with multi-echo (ME) sequences: magnitude and complex models [4, 27–29]. These models rely on the acquired data to perform an water/fat decomposition using a least-squares fitting procedure[30]. A few clinical applications of the magnitude model [5, 6, 31–37] and, to a lesser extent of the complex model [34, 37, 38] have proved these methods to be suitable alternatives for non-invasive *in-vivo* fat quantification. However, several methodological issues have largely been misunderstood [4, 7].

There are small spatial variations in the main magnetic field of an MR scanner, known as magnetic field inhomogeneities [4, 39–41]. They depend not only on hardware issues, but also on the sample that is being imaged. Magnetic field inhomogeneities, together with the chemical shift, influence the phase of the signal, introducing unexpected phase errors which can potentially increase the systematic errors associated with parameter estimation [4, 39]. Furthermore, such inhomogeneities tend to increase with the intensity of the main magnetic field, which implies that ultra-high field scanners ($B_0 > 3$ tesla (T)) are more susceptible to this problem. Although phase errors due to magnetic field inhomogeneities had been addressed, they are not, yet, well quantified [39]. The

complex model is very sensitive to this problem, since it takes phase information into consideration when estimating fat content. Magnitude model considers only magnitude data (discarding all phase information) and emerges as a simplified model that overcomes the estimation errors associated with magnetic field inhomogeneities [4, 27–29, 34]. Nevertheless, the latter model is characterized by inherent noise amplification. This, together with the fact that it contains no phase information implies that it is often unable to accurately estimate fat fractions over 50% [4, 37].

The influence of the relaxation effects ($T_1$ and $T_2^*$) is another confounding factor. Many studies discuss that the way that the relaxations are implemented in the models have a strong influence in the quantification, namely the $T_2^*$. It is well documented in the literature that when $T_2^*$ relaxation is ignored, highly biased estimations are obtained whereas in the presence of $T_2^*$ corrections the estimation is enhanced [7, 31]. Generally, two assumptions are made regarding $T_2^*$ relaxation constants:

1) Consider two independent $T_2^*$ constants for water and fat [7, 39, 42];

2) Assume only a common $T_2^*$ relaxation constant for both components [35, 40].

In certain conditions, the use of a single $T_2^*$ constant can improve fat quantification and avoid large errors [4, 27]. For instance, in advanced stages of NAFLD it is common to find iron overload in 40% of the patients [43, 44]. This shortens the values of $T_2^*$ leading to a much larger error in their estimation . Modelling the signal with only one $T_2^*$ relaxation constant is reported to be a way to surpass this situation [7, 36]. However, Chebrolu et al. (2010) questioned the validity of the assumption that $T_2^*$ of fat and water may be equal, given that there is no biological evidence in support of this statement. The same article indicates that for values of $T_2^*$ that are significantly different, larger errors emerge, especially when $T_2^*$ of fat and water are short [7]. In addition, it is known that spurious $T_1-$weighting images leads to an overestimation of fat since $T_1$ of fat is shorter than that for water; nevertheless, a way to overcome this problem is using small flip angles or dual flip angles during the acquisition [45].

In order to enhance fat quantification, some methodological improvements were proposed in recent years. A number of groups introduced MRS fat peaks when

modelling the signal [29, 30]. Hernando et al.(2012) proposed the mix-approach model in which the best of magnitude and complex models was taken into account. Although, good estimations were achieved by this model, phase errors remain a problem [34]. Finally, Heredita et al. (2012) developed a new methodology based on the analysis of liver-vessel cancelation artefact on in-phase and oppose-phase MRI images. This methodology shows that the presence of phase cancelation around the intra-hepatic vessels is a feature of ultra-high fat accumulation. However, phase cancelation is not observed in low values of fat content which implies that this approach is not complete in estimating a large range of fat accumulation [33].

Despite the advances in fat quantification based on chemical shift imaging, many issues remain quite unexplored. An important methodological issue is the choice of the TE combination to be used in data sampling. The latter is often empirical, and its impact in fat quantification with both the magnitude and complex models, remains to a large extent unknown [37]. Furthermore, the majority of chemical shift fat quantification procedures require accuracy evaluation by means of other techniques such MRS, which is particularly undesirable in clinical procedures [5, 6, 28, 29, 32].

# Chapter 2

# Materials and Methods

## 2.1 Signal models for fat quantification

Chemical shift imaging relies on the fact that hydrogen protons in water and fat molecules have different resonance frequencies. This technique uses the distinct water-fat phase shifts, generated at multiple echo times, to estimate the water and fat content in tissues on a voxel-by-voxel basis [37]. In general, voxels may contain different amounts of water and fat, as figure 2.1 suggests.

Each fat and water component generates signal with a given intensity. If signal intensity from both components can be sorted out correctly, then the precise amount of fat fraction, FF, can be calculated as

$$FF = \frac{S_f}{S_w + S_f} \tag{2.1}$$

where $S_w$ and $S_f$ are the signal intensities from water and fat, respectively [27].

In order to estimate $S_w$ and $S_f$, the signal from each voxel must be described by a suitable mathematical model. There are several factors to be taken into account when modelling the voxel signal:

1) A fundamental assumption of FF estimation is that water and fat are the only two signal-contributing chemical species [40];

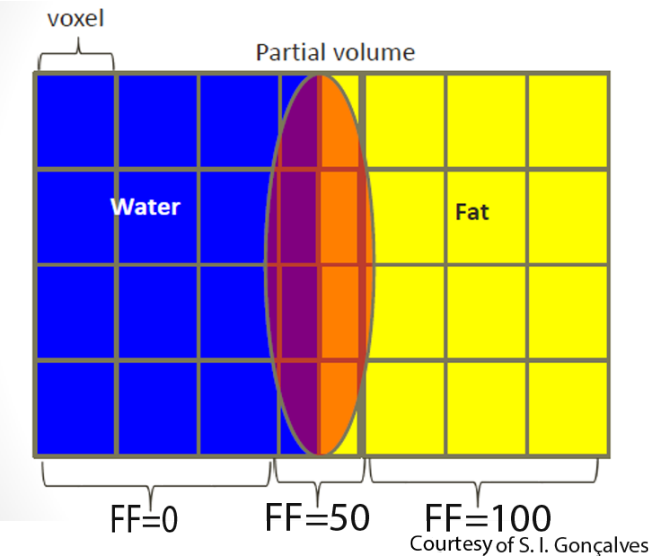


FIGURE 2.1: Schematic representation of a sample with voxels containing different amounts of water and fat.

2) Water and fat protons have different $T_2^*$ relaxation constants, which implies that the models must consider the signal intensity decay over time due to these constants [4];

3) Magnetic field inhomogeneities influence the signal phase and should also be considered when modelling the signal [4].

Several models have been proposed to describe the signal in chemical shift imaging. In the present study, the magnitude model and complex model are addressed.

### 2.1.1 Magnitude and complex models

A model vastly discussed in the literature is the estimation of fat from magnitude images. In this model, the magnitude of the total signal $|S|$ from any given voxel can be modelled as the sum of the signals from both water and fat components

$$|S| = \left| S_w e^{-TE/T_{2w}^*} + S_f e^{-TE/T_{2f}^*} e^{i\Delta\omega TE} \right| \tag{2.2}$$

Where TE represents the echo time, $S_w$ ($T_{2w}^*$) and $S_f$ ($T_{2f}^*$) are the signal intensities ($T_2^*$ relaxation constants) from water and fat respectively [28]. Parameter

$\Delta\omega$ is the phase angle due to the chemical shift effect and it is given, in radians, by

$$\Delta\omega = 2\pi\gamma\sigma B_0 \tag{2.3}$$

Here, $\gamma$ represents the gyromagnetic ratio, $\sigma$ is the chemical shift between fat and water and $B_0$ is the external magnetic field intensity [40].

If MR complex data is considered for fat quantification, i.e. if in addition to magnitude images, the phase information is also taken into account, then data modelling is slightly modified, when compared to 2.2. In this case, the signal from a voxel with water and fat, including the effects of $T_2^*$ relaxation, chemical shift and magnetic field inhomogeneities, can be modelled as

$$S = \left[S_w e^{-TE/T_{2w}^*} + S_f e^{-TE/T_{2f}^*} e^{i\Delta\omega TE}\right] e^{i\Delta\omega_0 TE} \tag{2.4}$$

where all constants are as defined in 2.2 [7]. Parameter $\Delta\omega_0 = 2\pi\gamma\Delta B_0$ is the frequency shift due to magnetic field inhomogeneities, $\Delta B_0$. The corresponding phase accumulation is then defined as $\phi = \Delta\omega_0 TE$ [40].

Magnitude and complex models can be implemented by considering that the $T_2^*$ relaxation constants of water and fat are different (dual-decay model) or by assuming the simplifying assumption that $T_{2w}^* = T_{2f}^*$ (single-decay model) [4, 35, 41]. In the latter case, equations 2.2 and 2.4 simplify to

$$|S| = \left|(S_w + S_f e^{i\Delta\omega TE}) e^{-TE/T_2^*}\right| \tag{2.5}$$

$$S = \left(S_w + S_f e^{i\Delta\omega TE}\right) e^{-TE/T_2^*} e^{i\Delta\omega_0 TE} \tag{2.6}$$

## 2.2 Theoretical and experimental work

### 2.2.1 Simulation studies

Simulations were conducted (for both single- and dual-decay models) to:

1) Determine the influence of different combinations of TE values in the estimation bias and error of FF, $T^*_{2w}$, and $T^*_{2f}$ in the presence of noise and using both magnitude and complex models;

2) Complex model: Determine the influence of phase errors due to magnetic field inhomogeneities in estimation bias of FF, $T^*_{2w}$, and $T^*_{2f}$;

3) Complex model: In the presence of noise and phase errors, study the variation of estimation bias and error with different combinations of TE values.

Data was simulated considering $T^*_{2w}$ =23.8ms, $T^*_{2f}$=18.5ms [4] and FF = 5%, 25%, 50% and 75%. Rician and Gaussian noise were added to magnitude and complex data respectively with relative noise amplitude (RNA) of 5% and 10%. Noise amplitude, NA, was calculated from the value of RNA according to

$$NA = max \begin{bmatrix} S_{0_w} \\ S_{0_f} \end{bmatrix} RNA \tag{2.7}$$

where $S_{0_w}$ and $S_{0_f}$ are the signal intensities for water and fat respectively, considering $B_0 = 0$.

Computations were conducted using software that was written in Matlab R2012a (Mathworks, Natick, Mass). The Levenberg-Marquart method (*lsqnolin* function in Matlab) was chosen for the non-linear fit (in a least-squares sense) of FF, $T^*_{2w}$, and $T^*_{2f}$ to the data.

#### 2.2.1.1 Noise studies

Monte Carlo simulations were conducted to evaluate the robustness of magnitude and complex models, in the presence of noise, for different combinations of TE values. Sample data was simulated at twelve different TEs at 3T. Each Monte Carlo simulation took 1000 different noise realizations into account. Noise realizations were extracted from a Rician distribution (in the case of magnitude data) and from a Gaussian distribution (in the case of complex data).

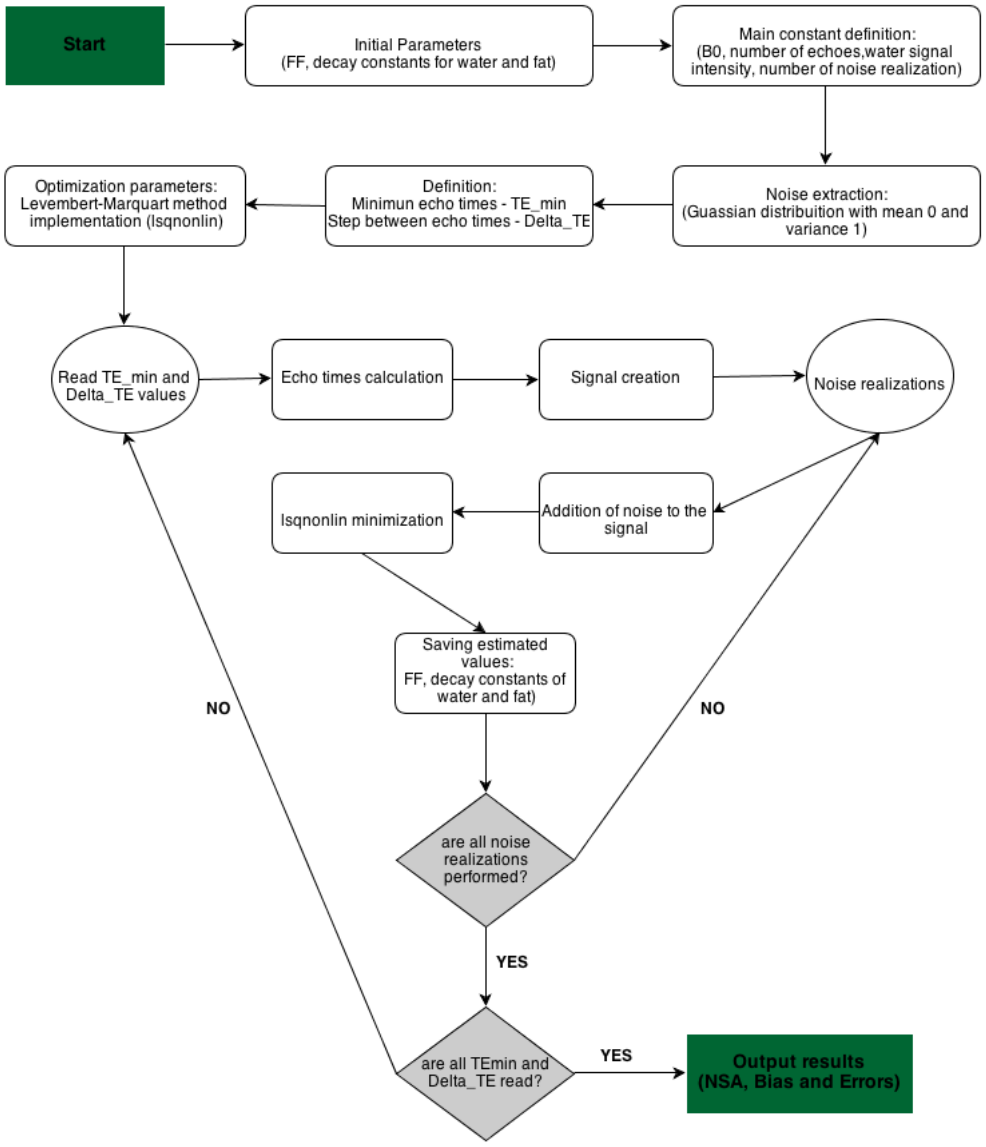


FIGURE 2.2: flowchart illustrating the major steps of the algorithm that was implemented to evaluate the behaviour of the models in the presence of noise.

The efficiency of each model to determine the FF was quantified using the number of signal averages (NSA) which is defined as

$$NSA = \sqrt{\frac{\sigma}{\sigma_E}} \tag{2.8}$$

Where $\sigma$ represents the noise standard deviation and $\sigma_E$ is the standard deviation associated with the estimation of $S_f$.

Besides NSA, two other measures were used to evaluate the models: Bias and Error. The Bias associated with a given parameter $X$ is defined as

$$BiasX = \frac{\bar{X_E} - X_t}{X_t} \times 100 \tag{2.9}$$

Where $\bar{X_E}$ is the mean of the estimates $X_E$ of all noise realizations, and $X_t$ is the true value of $X$. The bias of a given estimated parameter quantifies the error in parameter estimation due to the incompleteness of the model to describe the data. On the other hand, Error $X$ reflects the error in parameter estimation which results from the sensitivity of the model to noise. It is defined as

$$ErrorX = \frac{\sigma_{X_E}}{X} \times 100 \tag{2.10}$$

Where $\sigma_{X_E}$ is the standard deviation associated with $X_E$.

The biases and errors were computed for FF, $T^*_{2w}$ and $T^*_{2f}$. Results were represented as colour maps with the NSA, bias an errors expressed as function of $TE_{min}$ (TE minimum) and $\Delta$TE (step between TEs). The flowchart in figure 2.2 illustrates the major steps that were implemented in the algorithm for noise simulations.

#### 2.2.1.2 Influence of magnetic field inhomogeneities and noise on FF estimation using complex model

Model parameters were estimated for both single- and dual-decay models, without noise, at 400 different off-resonance frequencies, ranging from -200Hz to 200Hz and considering FFs of 5%, 25%, 50% and 75%. The simulations were performed for three distinct TE combinations: the clinical protocol and two TEs combinations that were chosen from the identification of TE-$\Delta$TE regions where both the bias and errors (in FF, $T^*_{2w}$ and $T^*_{2f}$) were minimized in the presence of noise (for single- and dual-decay models). All the remaining simulation parameters were equal to what was previously described.

*Echo times*:

1) Single-decay model: TEs of 3,00ms to 27,20ms in increasing steps of 2,20ms;

2) Dual-decay model: TEs of 2,80ms to 28,10ms in increasing steps of 2,30ms;

3) Clinical protocol: TEs of 2,46ms to 15,99ms in increasing steps of 1.23ms.

The biases in FF, $T^*_{2w}$ and $T^*_{2f}$ were obtained as function of off-resonance frequencies. The flowchart presented in figure 2.3 shows the algorithm that was implemented.

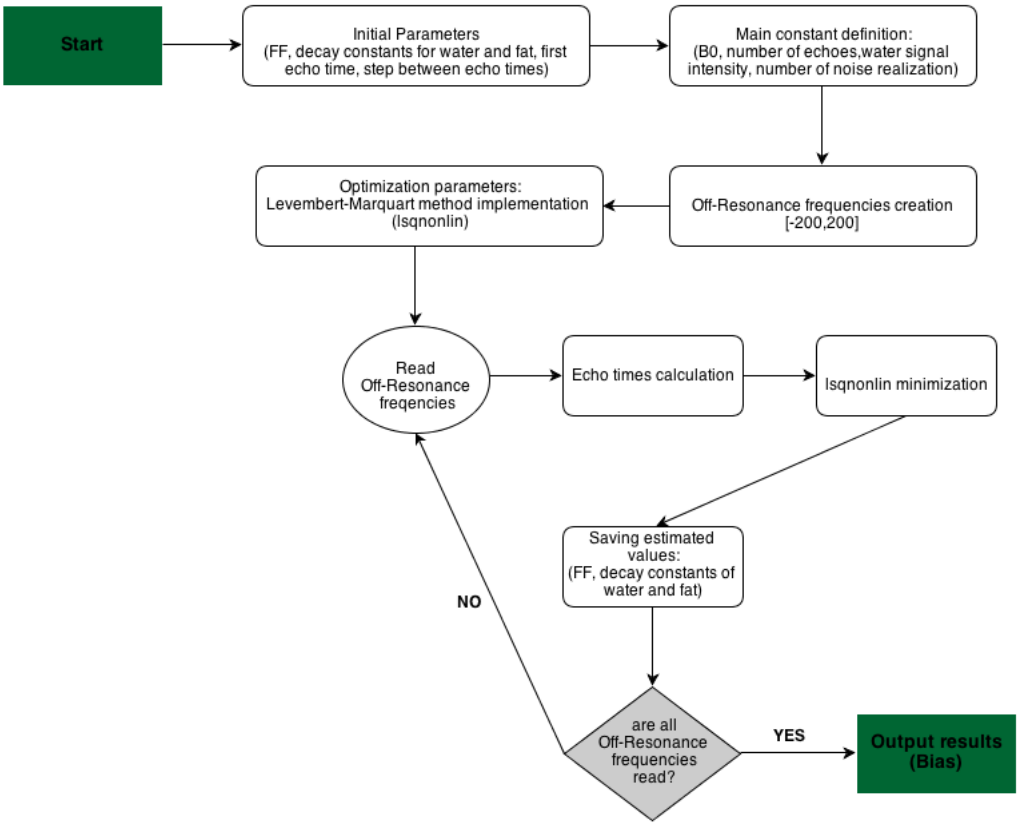


FIGURE 2.3: Flowchart illustrating the major steps of the algorithm that was implemented evaluate the influence of off-resonance frequencies on complex model FF estimations.

In order to evaluate the combined influence of noise and magnetic field inhomogeneities on FF estimation (with single- and dual-decay constants), a set of simulations, similar to those described above were computed. For each simulation, the $TE_{min}$ was kept fixed and equal to those indicated above. Estimation Bias and Error were plotted as colour maps as function of off-resonance frequencies and $\Delta$TE. Figure 2.4 shows the flowchart of the algorithm that was implemented for these computations.

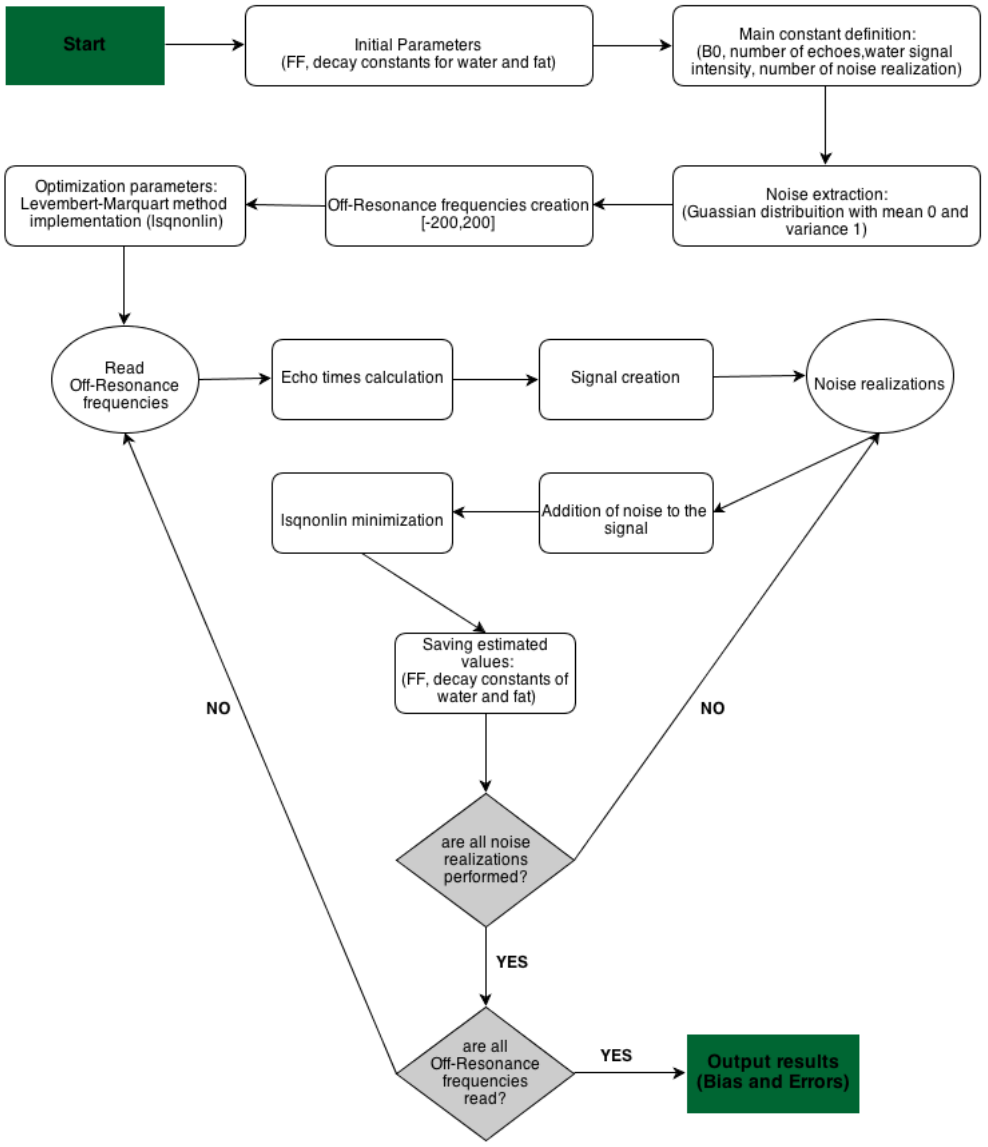


FIGURE 2.4: Flowchart illustrating the major steps of the algorithm that was implemented to evaluate the influence of noise and off-resonance frequencies on complex model FF estimations.

### 2.2.2 Fat quantification program

A program with a basic user interface was implemented in order to estimate FF, on a voxel-by-voxel basis, from *in-vivo* multi-echo gradient-echo (ME-GRE) data. In addition to FF, estimations for $T^*_{2w}$ and $T^*_{2f}$ can also be obtained. Results are obtained as parametric maps that are represented on the original dicom images (i.e. a voxel in a dicom image correspond to the same voxel in a parametric map). The flowchart in figure 2.5 indicates the major steps that are involved in the implementation of this program.

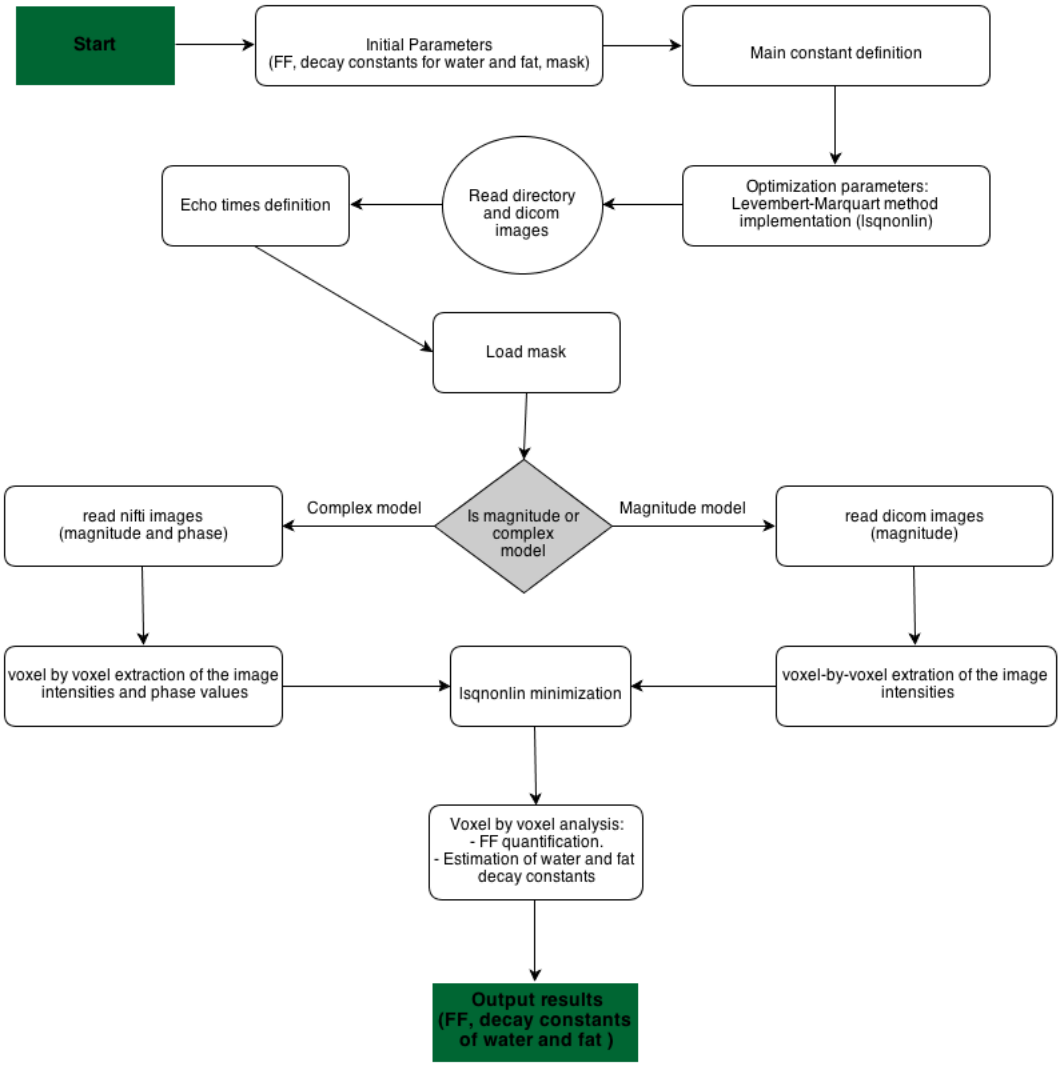


FIGURE 2.5: Flowchart illustrating the major steps of the algorithm that was implemented to estimate the FF on a voxel-by-voxel basis.

### 2.2.3 Experimental work

#### 2.2.3.1 Phantom construction

In order to experimentally validate the simulation results, a phantom consisting of 6 vials, containing a water-fat emulsion with different values of FF, was built. In order to minimize image artefacts, a homogeneous mixture has to be created. However, due to their polarity, water and fat do not mix spontaneously. There are several ways to solve this problem, but adding an emulsifier is the simplest one.

Emulsifiers are chemical compounds belonging to a major category of chemicals named as surfactants. Surfactants are organic molecules with amphipathic

characteristics. Due to this fact, the molecules of the emulsifier can interact either with polar and non-polar molecules. Therefore, the addition of an emulsifier, to a mixture of water and fat, allows the non-polar lipids to disperse into the polar molecules of water [46].

Due to their different densities, water and fat tend to separate. An easy way to avoid this is to add a stabilizer to the emulsion. Two major types of stabilizers are available: solid phase stabilizers and liquid phase stabilizers. Solid phase stabilizers work by creating a cross-linked matrix that traps the components and avoid the separation. Liquid phase stabilizers increase the viscosity of the emulsion thereby preventing the separation [46]. It should be stressed that even with the stabilizer, the separation continues to take place, but very slowly.

### Emulsions: choice of chemical compounds

*Oil:*

There are several vegetable oils which may be used in the phantom construction. The choice of the oil was based on several factors, namely chemical composition, toxicity, availability and price. Table 2.1 summarizes the information for four different oils.

| | Composition (over total total volume) | | | | Toxicity | Price | Availability |
|---|---|---|---|---|---|---|---|
| | Linoleic acid | Oleic acid | Stearic acid | Palmitic acid | | | |
| Soybean oil | 54% | 24% | 4% | 11% | non | 1,74 € / 1L (continente S.A.) | Now |
| **Penaut oil** | **27%** | **55%** | **4%** | **9%** | **non** | **3,25€ / 1L (Continente S.A.)** | **Now** |
| Sesame oil | 45% | 41% | 4% | 9% | non | 5,95€ / 250 mL (Celeiro) | Now |
| Canola oil | 22% | 62% | 4% | 11% | non | 7,95€ / 1L (Ayur.com) | Now |

TABLE 2.1: Fatty acids in the composition of four different vegetal oils. The toxicity, price and availability were also indicated.

One property of interest is the oil similarity to human fat in terms of fatty acid composition. To perform this comparison, a study by Kokatnur et al. (1979) was taken as reference [47]. In this study, the authors conduct an evaluation of the major fatty acids that are present in fat of the human buttock and in perirenal tissues. The relevant results are expressed in table 2.2.

In table 2.2, some fatty acids (myrist and palmitoleic acids) are neglected, since their percentage is minimal when compared with other fatty acids and they are not present in vegetable oils. In addition, focus was only to the perirenal because of its anatomical proximity to the liver. Comparing tables 2.1 and 2.2, we observe that peanut oil shows more proximity to human fat than any of the

| Composition (% by total fatty acids composition) | Age 25-34 | | Age 35-44 | |
|---|---|---|---|---|
| | Black | White | Black | White |
| **Palmitic acid** | 24,9 (24,5-25,3) | 24,3 (23,6-25,0) | 24,5 (24,1-24,9) | 24,4 (23,9-24,9) |
| **Stearic acid** | 8,2 (8,0-8,4) | 6,9 (6,4-7,6) | 7,8 (7,5-8,1) | 6,0 (5,6-6,4) |
| **Oleic acid** | 47,9 (47,5-48,3) | 47,3 (46,0-48,6) | 49,2 (48,7-49,7) | 49,7 (49,0-50,4) |
| **Linileic acid** | 12,1 (11,7-12,5) | 12,7 (11,6-13,8) | 11,1 (10,6-11,6) | 11,0 (10,2-11,8) |

TABLE 2.2: Fatty acid composition of fat in the perirenal region for different races and ages. Adapted from [47]

other oils. It is commonly used in cooking and can be purchased from any food store at a relatively low price. Furthermore, peanut oil has been previously used in phantoms from other research groups thus providing more information about its use in phantom construction [38, 45]. Taking all this into account, peanut oil emerged as an optimal choice.

*Emulsifier:*

As emulsifier agent we used the anionic surfactant sodium dodecyl sulphate (SDS). SDS is non-toxic and it was readily available.

*Stabilizer:*

Based on the literature two stabilizers were considered: agar and gelatine. Gelatine (solid phase stabilizer) is a triplex helix compound derived from hydrolysed collagen and when in contact with water forms a gel which prevents phase separation [48]. Agar is a polysaccharide extracted from red-purple marine algae and is used as a growing medium [49]. Gelatine was chosen over agar due to its capacity to easily crosslink the amine groups by an aldehyde [48]. Formaldehyde was the chosen aldehyde for this purpose.

### Preparation

| | Vial 1 | Vial 2 | Vial 3 | Vial 4 | Vial 5 | Vial 6 |
|---|---|---|---|---|---|---|
| Vial volume (mL) | 20 | 20 | 20 | 20 | 20 | 20 |
| Water and Fat Volume (mL) | 18 | 18 | 18 | 18 | 18 | 18 |
| Percent of oil (%) | 0 | 5 | 10 | 25 | 50 | 100 |
| Percent of Water (%) | 100 | 95 | 90 | 75 | 50 | 0 |
| Volume of oil (mL) | 0,00 | 0,90 | 1,80 | 4,50 | 9,00 | 18,00 |
| Volume of Water (mL) | 18,00 | 17,10 | 16,20 | 13,50 | 9,00 | 0,00 |
| Volume of Emulsifier (g) | 0,43 | 0,43 | 0,43 | 0,43 | 0,43 | 0,43 |
| Volume of Formalin (mL) | 0,16 | 0,16 | 0,16 | 0,16 | 0,16 | 0,16 |
| Weight Gelatin (g) | 2,99 | 2,99 | 2,99 | 2,99 | 2,99 | 2,99 |
| Total Volume of water and oil (mL) | 18,00 | 18,00 | 18,00 | 18,00 | 18,00 | 18,00 |
| Total Volume (mL) | 18,59 | 18,59 | 18,59 | 18,59 | 18,59 | 18,59 |

TABLE 2.3: Composition and final volume of each vial.

A protocol, based on the report from Parlato et al. (2009) was designed in order to prepare the emulsion and build the phantom:

1) The amount of each component of the emulsion was calculated in a Microsoft Excel spread sheet. The major parameters to consider here were the volume of the vials and desired fat percentage. The composition of each vial is given in table 2.3;

2) The desired volumes of water, oil and formalin were measured; gelatine and emulsifier were weighted;

3) A 100mL solution of sodium dodecyl sulphate was prepared;

4) The gelatine was added while the solution was heating using a magnetic stirrer hotplate [50];

5) When the solution reached a temperature between $65^o - 93^o$ the peanut oil was added;

6) The mixture was then left to cool down and when it reached a temperature between $37^o - 49^o$, formalin was added;

7) The emulsion was homogenised, by means of a homogenizer, during 2 minutes with 1 minute rest interval;

8) Finally, the emulsion was rapidly cooled in ice in order to form a gel and prevent phase separation.

This procedure was repeated 6 times; one for each vial.

After all emulsions were prepared, the vials were placed side by side on a frame. Figure 2.6 sketches the phantom final result, indicating the values of FF in each vial.

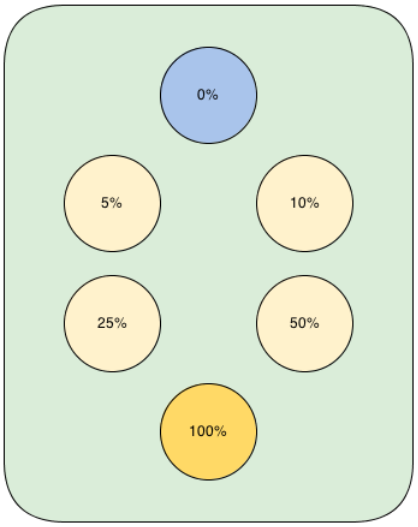


FIGURE 2.6: Schematic representation of the phantom. Values of FF are shown within each vial.

#### 2.2.3.2 Phantom measurements

The phantom was imaged in a 3T whole-body MRI scanner (Siemens Magnetom Trio, Erlangen, Germany), using a ME-GRE sequence with 12 TEs. Further imaging parameters were: $FOV = 165 \times 220mm$, $TR = 32ms$, $\alpha = 10^o$, Acquisition Matrix= $192 \times 115$ , 2 slices 10mm thick. Magnitude and phase images were acquired with 5 different combinations of TE values:

1) Clinical protocol: TEs of 2,46ms to 15,99ms in increasing steps of 1.23ms;

2) TEs of 3,00ms to 28,3ms in increasing steps of 2,30ms;

3) TEs of 2.60ms to 16,46ms in increasing steps of 1,26ms;

4) TEs of 3,00ms to 27,20ms in increasing steps of 2,20ms;

5) TEs of 2,80ms to 28,10ms in increasing steps of 2,30ms.

### Image processing

Phase images were exported from the MR scanner in dicom format, where phase values were integers ranging from -2048 to 2048. When these images are loaded into a dicom reader, the image intensity, $I$, is rescaled according to:

$$I = RescaleSlope \times I_{raw} + RescaleIntercept \tag{2.11}$$

Where *RescaleSlope* and the *RescaleIntercept* are two main fields in any dicom header. For Siemens scanners, the value of these fields is 2 and -4096 respectively. When re-scaling takes place, phase values, from 0 to 4096, correspond to real values falling in the interval [0, $2\pi$]. Phase values are wrapped, with the instantaneous phase values, $\phi(t)$, confined to be in $[-\pi, \pi]$ or [0, $2\pi$]. Therefore, all phase values that are outside these intervals are folded back. In order to surpass this problem and determine the correct phase values, the application of phase unwrapping algorithms is needed.

*Major steps for phase image pre-processing:*

1) Scale image intensity according to 2.11 using Matlab;
2) Conversion of phase images from dicom to nifti format [51], using *dcm2nii* utility [52];
3) Application of the rescaling using FSL [53];
4) Creation of a mask containing only the pixels within the vials. Mask magnitude images using *FSL's Bet*;
5) Phase unwrapping using *FSL's prelude*.

Images were then processed using the program described in section 2.2.2. Over each vial, a region of interest (ROI) was defined where FF quantification was performed and results were obtained as parametric maps. In addition, plots of the true FF against the estimated FF were also obtained.

#### 2.2.3.3 *In-vivo* experiments

In order to perform *in-vivo* experiments, the Diamarker project population, consisting of 37 controls (23 females, mean age of 49±7) and 32 patients (20 females, mean age of 60±8), was considered. The patient group is composed by subjects with type II diabetes, while control group consists of subjects without history of neuropsychiatric, renal, liver, heart, ocular or any other severe non-age related disease. From this population seven controls and seven patients were enrolled in our study. Control subjects were chosen with the prior information that no liver fat accumulation was observed. In opposition, the chosen patients were known to have considerable fat accumulation.

Prior to the present work, breath-hold images were acquired on a whole-body MRI scanner (Siemens Magnetom Trio, Erlangen, Germany) using ME-GRE sequences with twelve echoes and acquisition parameters: $FOV = 400 \times 400mm$, TR of 30ms and clinical protocol TEs. In this procedure, a single slice 10mm thick, was acquired.

Fat quantification was performed for 7 controls and 7 patients. Only magnitude models were used for this purpose, since no phase images had been acquired. For each image, a mask was applied on the actual abdominal structures (ROIs), as a means to discard the background noise. Finally, all results were obtained in a form of parametric maps of the abdominal region and representing FF values on a voxel-by-voxel basis.

# Chapter 3

# Results

## 3.1 Simulations studies

### 3.1.1 Noise studies

The variation of NSA with TE-ΔTE, for magnitude and complex models, is displayed in figure 3.1 for a RNA of 5%.

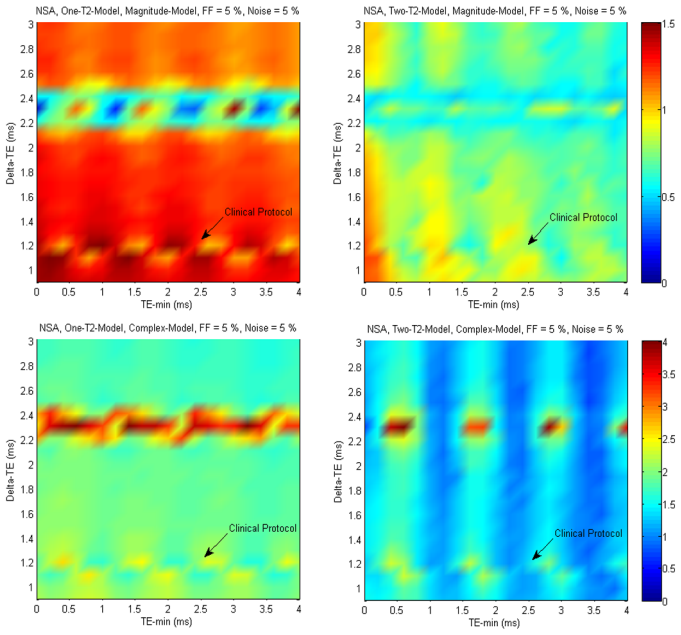


FIGURE 3.1: NSA values obtained with magnitude single- and dual-decay model (above). NSA values for complex single- and dual-decay model (below). All values of NSA computed for a FF of 5% and a RNA of 5%.

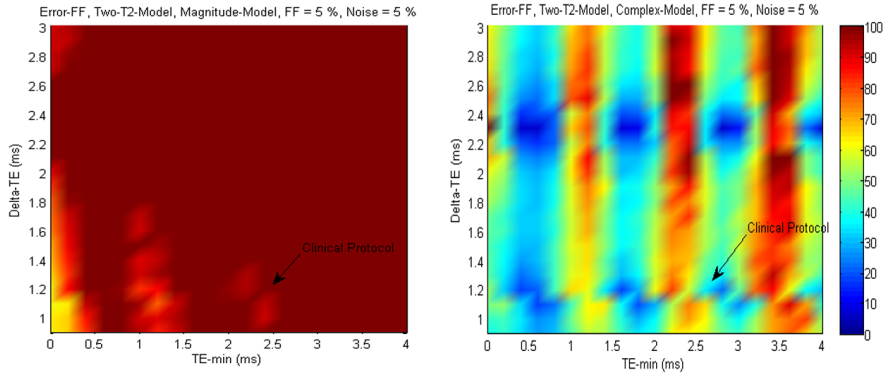


FIGURE 3.2: FF estimation error for magnitude (left) and complex (right) model. Both models were implemented with dual-decay constants, FF equal to 5% and RNA of 5%. The error corresponding to the TE-ΔTE combination that is used in the clinical protocol is indicated with a black arrow.

From the comparison of the colour maps in figure 3.1, it becomes evident that magnitude model is more sensitive to the assumptions that are considered for $T_2^*$ relaxation constants: generally, NSA values above 1 for single-decay model and below 1 otherwise. In opposition, the complex model has higher NSA values: generally, above 2 when implemented with dual-decay constants and below 2 otherwise. Hence, the fitting performed with single-decay constants appears to be more robust to noise in both models. The clinical TE-ΔTE combination is indicated. This combination is not optimal, falling in a region where NSA is not maximized. Furthermore, the results for a RNA of 10% (not shown) are similar.

The colour maps in figure 3.2 show the dependence of FF estimation error on the combinations of TEs that are used to sample the signal, for both magnitude and complex models, implemented with dual-decay constants. In the dual-decay model, $T^*_{2water}$ and $T^*_{2fat}$ are different, whereas in the single-decay model the simplification $T^*_{2water}$=$T^*_{2fat}$ is considered. A straightforward observation, which is common to all other parameter combinations that were used in the simulations, is that there are combinations of TE which yield a lower error associated with FF estimation -TE-ΔTE best combinations.

Figure 3.3 extends the results for different values of FF (25%, 50%, 75%). The number of TE-ΔTE combinations that minimize FF error increase with the value of FF. The performance of the complex model is better than that of the magnitude model since overall, the error in FF is smaller than that obtained with the magnitude model: almost all errors are below 10% for all FF.

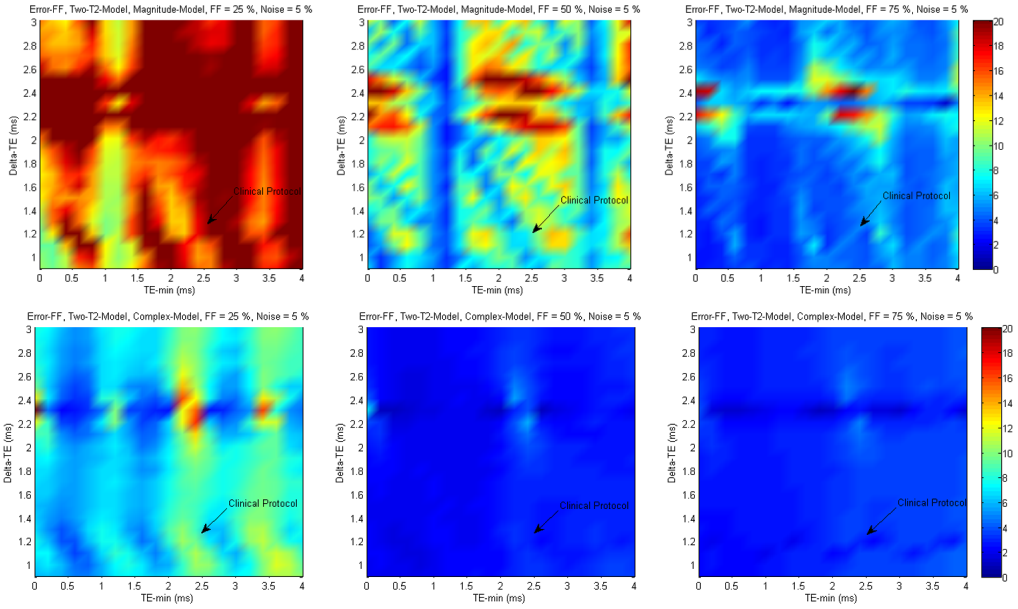


FIGURE 3.3: FF estimation error for magnitude (above) and complex (below) model. Both models were implemented with dual-decay constants, FF equal to 5% and RNA of 5%.

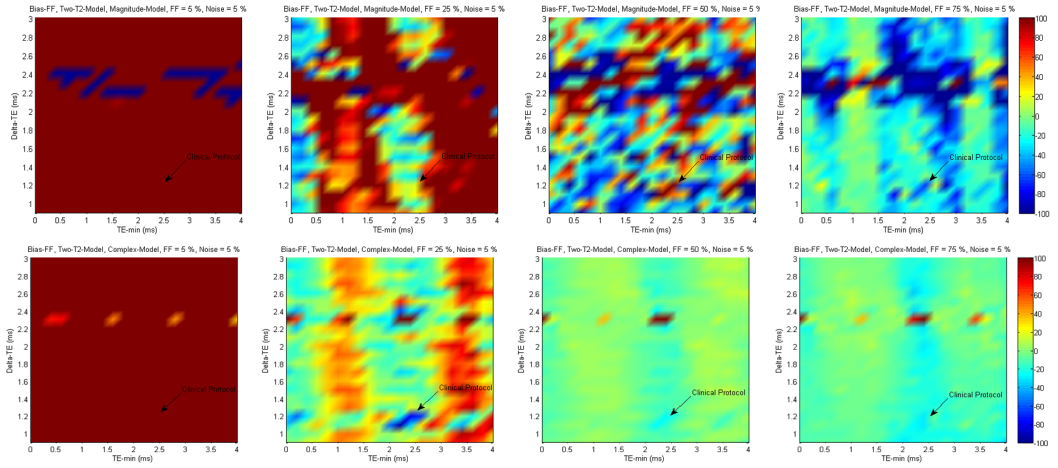


FIGURE 3.4: FF estimation bias for different values of FF, performed with magnitude (above) and complex (below) models, dual-decay constants and RNA of 5%.

Results of the estimation bias are shown in figure 3.4. Similarly to the FF estimation error, also here the complex model performs better than the magnitude model. For all FF values above 5%, minimum estimation bias obtained with the complex model lie close to 0% whereas for the magnitude models that is not the case. For a FF of 5%, both models fail to yield unbiased estimations of FF.

Figure 3.5 shows a comparison between the performances of complex and magnitude models using single-decay constants. When comparing figures 3.3 and 3.5 one observes that the way by which relaxations effects are included in the

model strongly affect the FF estimation error. Particularly for the magnitude model, considering $T^*_{2water}$=$T^*_{2fat}$ decreases the estimation error for all FF values except that of 5%. In general, the complex model performs better than the magnitude model, even for FF=5% where complex dual-decay model achieves lower error. Finally, complex model appears to be more robust, in terms of the estimation error, when implemented with two decay constants.

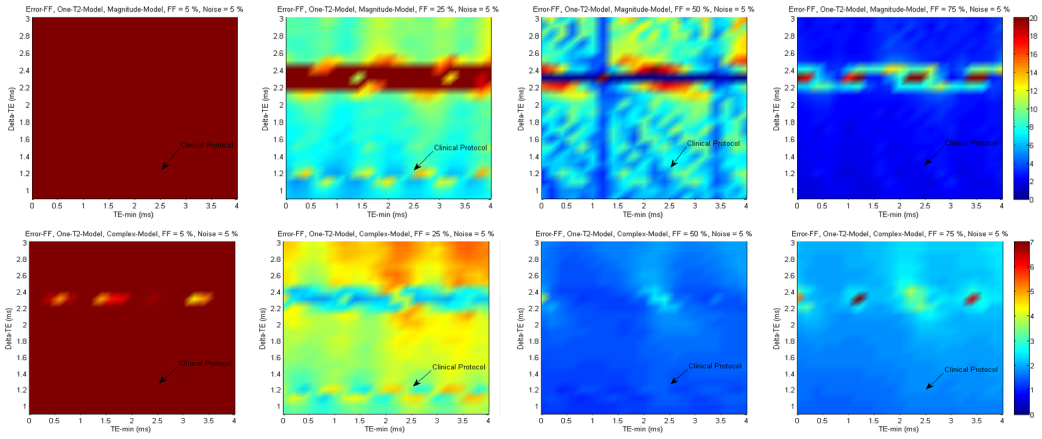


FIGURE 3.5: FF estimation errors for different values of FF, estimated with magnitude (above) and complex (below) models with single-decay constants. RNA of 5%.

The bias obtained for the magnitude single-decay model is shown in figure 3.6. When compared to figure 3.4, we observe that magnitude single-decay model originates a more biased estimation of FF. However, for FFs of 50%, magnitude model presents some regions of bias between -10% and 10%. The problem here is that it is difficult to find a TE-ΔTE combination where both FF error and bias are minimized. The bias results for complex model are not represented since their values are generally negative and extremely high, lying beyond -100%. This is an unexpected result, which illustrates some difficulties of the complex in describing the data when implemented with only one decay constant.

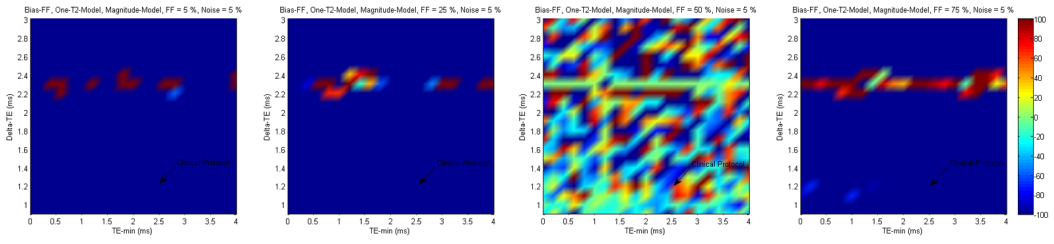


FIGURE 3.6: FF estimation bias for different values of FF, estimated with magnitude single-decay model and RNA of 5%.

It is worth mentioning that, in all cases, the TE-ΔTE combination that is used in the clinical protocol falls on regions of high errors and biases. This suggests that the clinical protocol is not optimized for FF estimation.

The error and bias associated with $T_2^*$ constants (results not shown) indicate that the single-decay magnitude model performs better than the dual-decay magnitude model. For low values of FF (5% and 25%), the error and bias in the estimates of $T_{2fat}^*$ are high and more TE-ΔTE combinations are observed to minimize the error and bias of $T_{2water}^*$. In contrast, for high values of FF (75%) the opposite is observed: lower error and bias for $T_{2fat}^*$ and higher error and bias for $T_{2water}^*$. The complex model shows a similar behaviour. In fact, for low values of FF, the complex single-decay model is better, but as the values of FF increase, the dual-decay model yields more TE-ΔTE combinations in which the error and bias are minimized.

From the previous results, four alternative TE combinations were chosen to minimize the errors and biases, particularly in FF, associated with each model. Table 3.1 indicates these combinations.

| | | **Magnitude Model** | **Complex Model** |
|---|---|---|---|
| **Single Decay Model** | $TE_{min}$ (ms) | 3,00 | 3,00 |
| | Δ TE (ms) | 2,30 | 2,20 |
| **Dual Decay Model** | $TE_{min}$ (ms) | 2,60 | 2,80 |
| | Δ TE (ms) | 1,26 | 2,30 |

TABLE 3.1: Alternative TE-ΔTE combinations for magnitude and complex models with single- and dual-decay constants.

The choice of the values in 3.1 relied on the identification of TE-ΔTE regions where the error and bias associated with $T_{2water}^*$, $T_{2fat}^*$ and FF respectively were minimized. However, this implies that there are a total of six parameters that must be accounted for. This means that the chosen TE-ΔTE combinations are a compromise between the minimization of $Error_{T_{2water}^*}$, $Error_{T_{2fat}^*}$, $Error_{FF}$, $Bias_{T_{2water}^*}$, $Bias_{T_{2fat}^*}$ and $Bias_{FF}$. Tables 3.2 and 3.3 summarize the biases and errors in the various parameters associated with the chosen combinations. Tables 3.4 and 3.5 present the same information for the clinical protocol.

| | Bias $T^*_2$ water (%) | | | | Bias $T^*_2$ fat (%) | | | | Bias FF (%) | | | | Error $T^*_2$ water (%) | | | | Error $T^*_2$ fat (%) | | | | Error FF (%) | | | |
|---|---|---|---|---|---|---|---|---|---|---|---|---|---|---|---|---|---|---|---|---|---|---|---|---|
| **Fat Fraction (%)** | **5** | **25** | **50** | **75** | **5** | **25** | **50** | **75** | **5** | **25** | **50** | **75** | **5** | **25** | **50** | **75** | **5** | **25** | **50** | **75** | **5** | **25** | **50** | **75** |
| **Single Decay Model** | 1,00 | 0,00 | -10,00 | -20,00 | 30,06 | 29,08 | 16,28 | 2,79 | -960,96 | 246,59 | 0,00 | 103,70 | 8,86 | 8,77 | 4,44 | 1,34 | 11,40 | 11,28 | 5,71 | 1,73 | 47,57 | 27,27 | 0,00 | 2,49 |
| **Dual Decay Model** | 2,00 | 2,00 | 4,00 | 83,00 | 2325,93 | 71,48 | 4,22 | 2,07 | 3356,51 | 1,86 | -40,69 | -25,59 | 15,58 | 16,03 | 25,08 | 687,94 | 4177,95 | 502,84 | 20,34 | 11,82 | 99,56 | 14,80 | 6,94 | 3,95 |

TABLE 3.2: Estimation errors and bias associated with the chosen TE combinations for magnitude model, both with single- and dual-decay constants.

| | Bias $T^*_2$ water (%) | | | | Bias $T^*_2$ fat (%) | | | | Bias FF (%) | | | | Error $T^*_2$ water (%) | | | | Error $T^*_2$ fat (%) | | | | Error FF (%) | | | |
|---|---|---|---|---|---|---|---|---|---|---|---|---|---|---|---|---|---|---|---|---|---|---|---|---|
| **Fat Fraction (%)** | **5** | **25** | **50** | **75** | **5** | **25** | **50** | **75** | **5** | **25** | **50** | **75** | **5** | **25** | **50** | **75** | **5** | **25** | **50** | **75** | **5** | **25** | **50** | **75** |
| **Single Decay Model** | 0,00 | -4,00 | -11,00 | -18,00 | 28,68 | 23,35 | 14,30 | 6,03 | -676,65 | -557,52 | -366,38 | -180,70 | 8,78 | 7,00 | 4,12 | 4,68 | 11,30 | 9,00 | 5,30 | 6,02 | 16,14 | 3,07 | 1,54 | 2,21 |
| **Dual Decay Model** | 1,00 | 1,00 | 1,00 | 1,00 | 0,10 | 0,12 | 0,05 | 0,00 | 46,43 | 0,74 | -0,67 | 0,38 | 8,69 | 8,57 | 8,19 | 12,13 | 19,74 | 2,11 | 1,28 | 1,17 | 7,54 | 2,90 | 1,83 | 1,57 |

TABLE 3.3: Estimation errors and bias associated with the chosen TE combinations for complex model, both with single- and dual-decay constants.

| | Bias $T^*_2$ water (%) | | | | Bias $T^*_2$ fat (%) | | | | Bias FF (%) | | | | Error $T^*_2$ water (%) | | | | Error $T^*_2$ fat (%) | | | | Error FF (%) | | | |
|---|---|---|---|---|---|---|---|---|---|---|---|---|---|---|---|---|---|---|---|---|---|---|---|---|
| **Fat Fraction (%)** | **5** | **25** | **50** | **75** | **5** | **25** | **50** | **75** | **5** | **25** | **50** | **75** | **5** | **25** | **50** | **75** | **5** | **25** | **50** | **75** | **5** | **25** | **50** | **75** |
| **Single decay model** | 1,00 | -2,00 | -11,00 | -19,00 | 30,28 | 26,42 | 14,58 | 4,67 | -704,96 | -458,16 | -67,83 | -147,93 | 12,93 | 10,95 | 5,89 | 5,62 | 16,63 | 14,08 | 7,58 | 7,23 | 56,08 | 8,02 | 5,09 | 2,06 |
| **Dual decay Model** | 2,00 | 0,00 | 17,00 | 181,00 | 3170,49 | 599,44 | -5,38 | 2,04 | 3481,53 | 15,76 | 170,24 | -63,15 | 13,29 | 16,14 | 36,46 | 1405,99 | 4721,05 | 2076,39 | 24,29 | 10,03 | 113,28 | 17,79 | 7,14 | 4,98 |

TABLE 3.4: Estimation errors and biases associated with the clinical protocol combination for magnitude model, both with single- and dual-decay constants.

| | Bias $T^*_2$ water (%) | | | | Bias $T^*_2$ fat (%) | | | | Bias FF (%) | | | | Error $T^*_2$ water (%) | | | | Error $T^*_2$ fat (%) | | | | Error FF (%) | | | |
|---|---|---|---|---|---|---|---|---|---|---|---|---|---|---|---|---|---|---|---|---|---|---|---|---|
| **Fat Fraction (%)** | **5** | **25** | **50** | **75** | **5** | **25** | **50** | **75** | **5** | **25** | **50** | **75** | **5** | **25** | **50** | **75** | **5** | **25** | **50** | **75** | **5** | **25** | **50** | **75** |
| **Single decay model** | 1,00 | -2,00 | -10,00 | -18,00 | 30,17 | 26,30 | 15,53 | 6,06 | -747,91 | -610,49 | -449,80 | -224,38 | 12,86 | 10,68 | 6,07 | 5,99 | 16,54 | 13,74 | 7,81 | 7,71 | 23,41 | 3,77 | 1,44 | 1,81 |
| **Dual decay Model** | 2,00 | 1,00 | 1,00 | 12,00 | 122,61 | 7,88 | 1,28 | 1,53 | 979,64 | -75,30 | -26,51 | -28,86 | 13,21 | 12,97 | 12,40 | 85,49 | 755,68 | 26,45 | 6,67 | 6,56 | 57,21 | 9,64 | 3,11 | 2,98 |

TABLE 3.5: Estimation errors and biases associated with the clinical protocol combination for complex model, both with single- and dual-decay constants.

### 3.1.2 Influence of magnetic field inhomogeneities and noise on FF estimation using complex model

Figures 3.7 and 3.8 illustrate the complex model behaviour under the influence of $B_0$ inhomogeneities for different TEs combinations. Our results demonstrate that in the presence of magnetic field inhomogeneities (in the plots expressed as off-resonance, $\Delta F_0$, in Hz), the estimation of all parameters and that of FF in particular, are highly biased. For the remaining FF values (results not shown), a similar behaviour is observed. However, complex dual-decay model appears to be slightly more resilient to phase errors: low bias is achieved even for high off-resonance frequencies, particularly for low FFs .

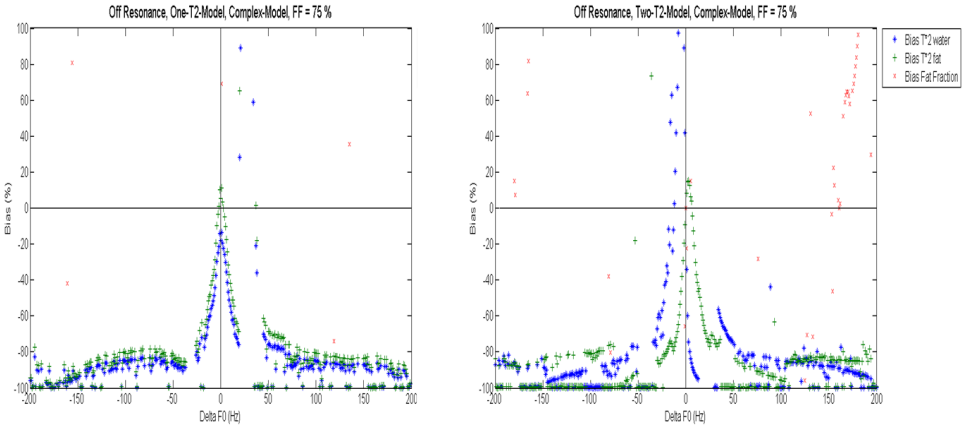


FIGURE 3.7: Influence of magnetic field inhomogeneities on FF, $T^*_{2water}$ and $T^*_{2fat}$ bias for single- and dual-decay complex models. Simulation parameters: FF=75% for single- and decay-model using the alternative protocol.

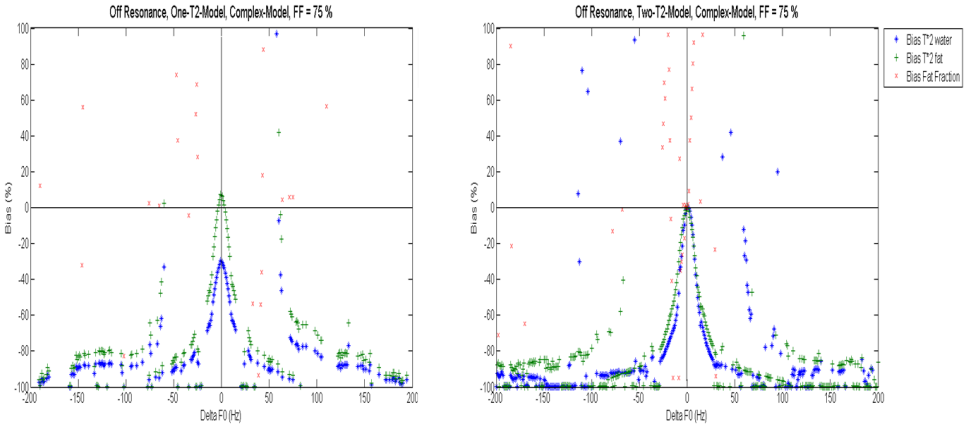


FIGURE 3.8: Influence of magnetic field inhomogeneities on FF, $T^*_{2water}$ and $T^*_{2fat}$ bias for single- and dual-decay complex model. Simulation parameters: FF=75% for for single- and decay-model using the clinical protocol

The influence of noise and magnetic field inhomogeneities in FF estimation is illustrated in figures 3.9 (Error) and 3.10 (Bias) for the dual-decay model and

considering TE-ΔTE values that according to table 3.1 minimize both FF bias and error in the presence of noise only.

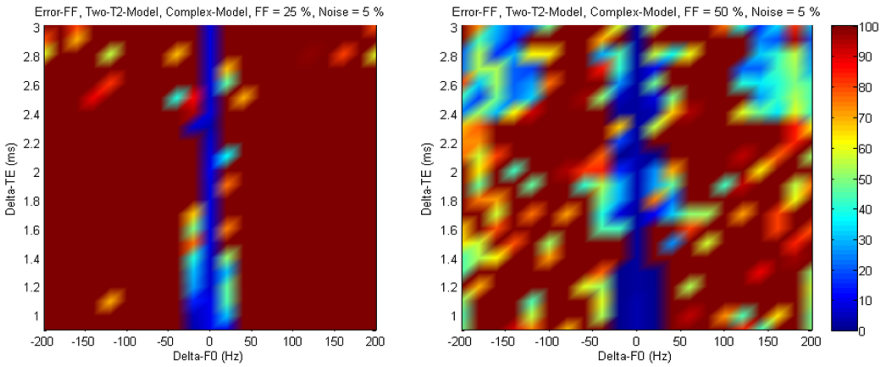


FIGURE 3.9: FF estimation error in the presence of noise and magnetic field inhomogeneities on complex dual-decay model. $TEmin$ of 2.80ms.

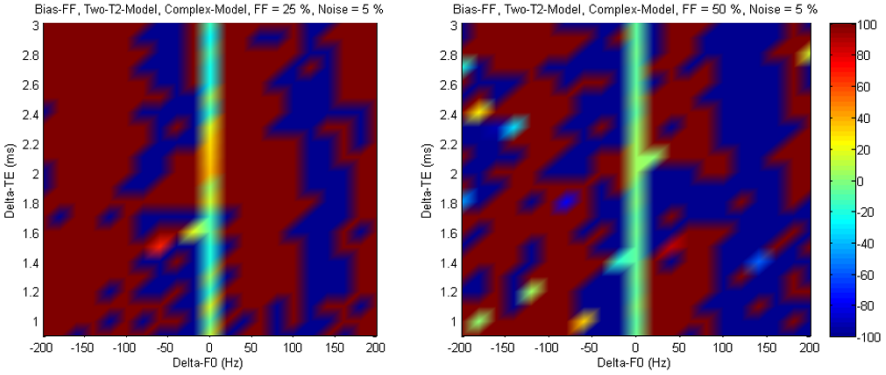


FIGURE 3.10: FF estimation bias in the presence of noise and magnetic field inhomogeneities on complex dual-decay model. $TEmin$ of 2.80ms.

In figures 3.9 and 3.10 it is notorious that in the presence of both magnetic field inhomogeneities and noise, the performance of the complex model becomes clearly worse. This is translated into high values of FF bias and error for off-resonance frequencies.

## 3.2 Phantom measurements

Figure 3.11 shows the phantom that was built to test the simulation results in a controlled setting. Visual inspection as well as the MR images suggested that the emulsions in all tubes were homogeneous, at least at a macroscopic scale.

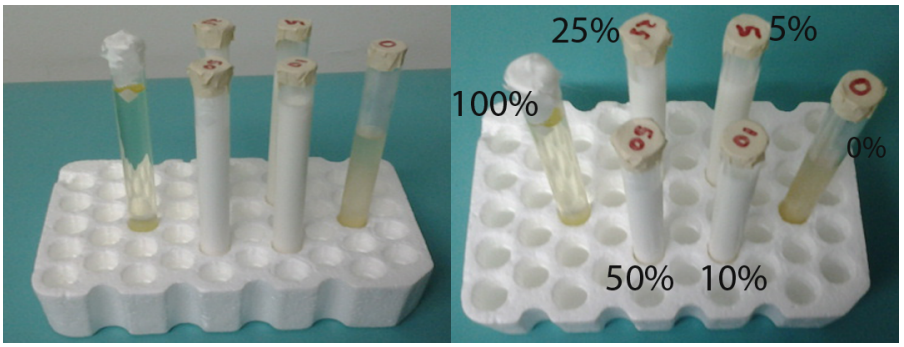


FIGURE 3.11: Phantom for FF quantification with indication of the relative amount of fat per vial.

### 3.2.1 Clinical protocol

Figure 3.12 shows a phantom coronal image acquired using the clinical protocol. FF quantification with the magnitude model with single- and dual-decay constants is represented as parametric maps. Moreover, a plot of the true FF against the estimate FF, computed as the average estimated FF in each vial, is also shown for clarity.

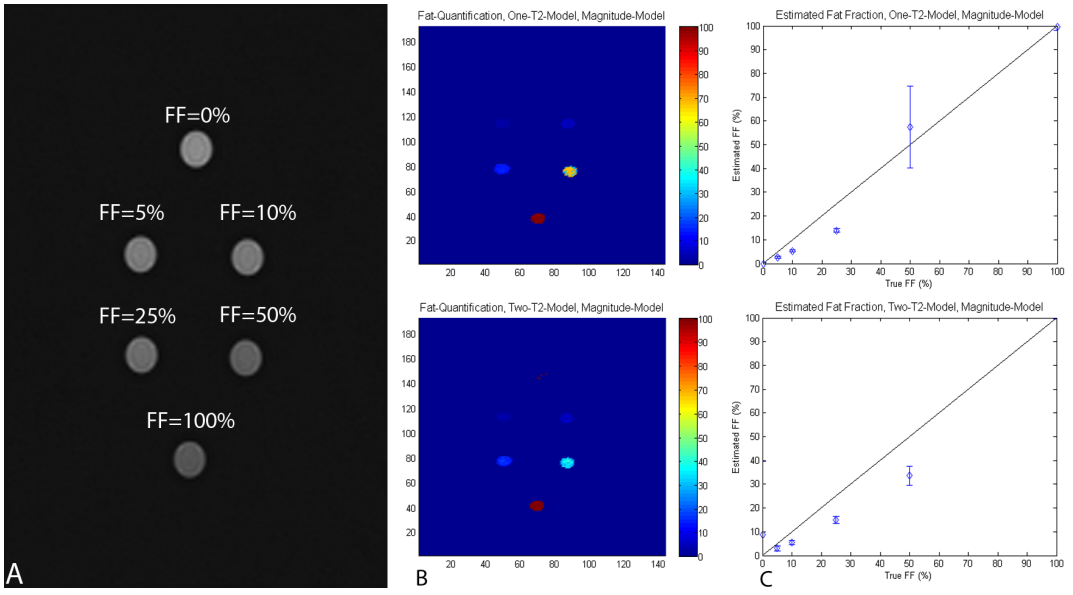


FIGURE 3.12: Phantom FF quantification with the magnitude model implemented with both single- and dual-decay constants. Coronal image of the phantom, obtained with the clinical protocol (A), parametric map of FF (B) and plot of the true FF against the estimated FF (C).

We observe that for both magnitude single- and dual-decay models a good estimation for low FF (0% and 5%) as well as for a FF of 100% is obtained. For intermediate values, the estimation of FF in the vials is more biased. Nevertheless, for FF=50% the estimated FF value (single-decay model) is very close to its true value but, with a high associated error. The comparison of figure 3.12 with the same results for another coronal slice (results not shown) shows

that there is a disparity FF estimation from one slice to another (especially for the dual-decay model). This observation may indicate the presence of emulsion inhomogeneities along the vials, which in turn may reduces the sample quality leading to less accurate estimations. The magnitude dual-decay model appears to be more sensitive to such problem.

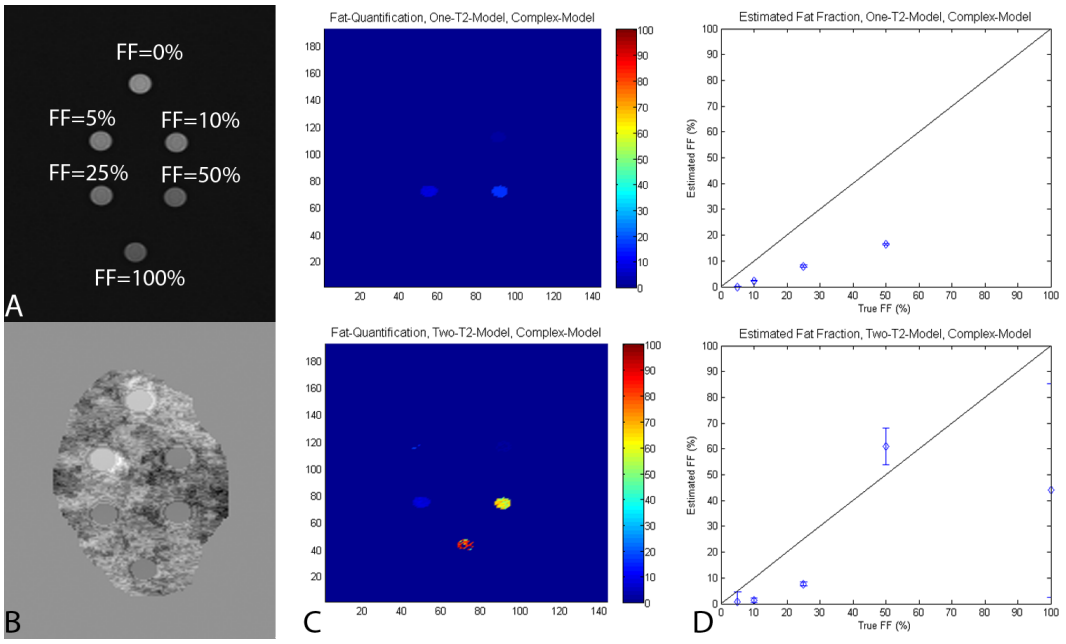


FIGURE 3.13: Phantom FF quantification performed with complex model, implemented with both single- and dual-decay constants. Acquired magnitude (A) and phase (B) images of a slice using the clinical protocol, parametric map of FF quantification (C) and plot of the true FF against the estimated FF (D).

The FF was also estimated using the complex model with single- and dual-decay constants. The result for a coronal slice is presented in figure 3.13.

Complex models show a less accurate quantification. Interestingly, though, the errors associated with each of estimations are smaller than those of the magnitude model, the majority of our estimates are underestimated, particularly for the single-decay model. This observation is in contradiction to the simulation results: although, theoretically best results are obtained using the complex models, the same is not truth in practical approaches.

### 3.2.2 Magnitude model alternative combinations

From section 3.1.1, two alternative combinations were chosen and known to minimize the error and bias in the magnitude model. These combinations were

tested using the phantom and results are shown in figures 3.14 and 3.15 for two distinct coronal slices.

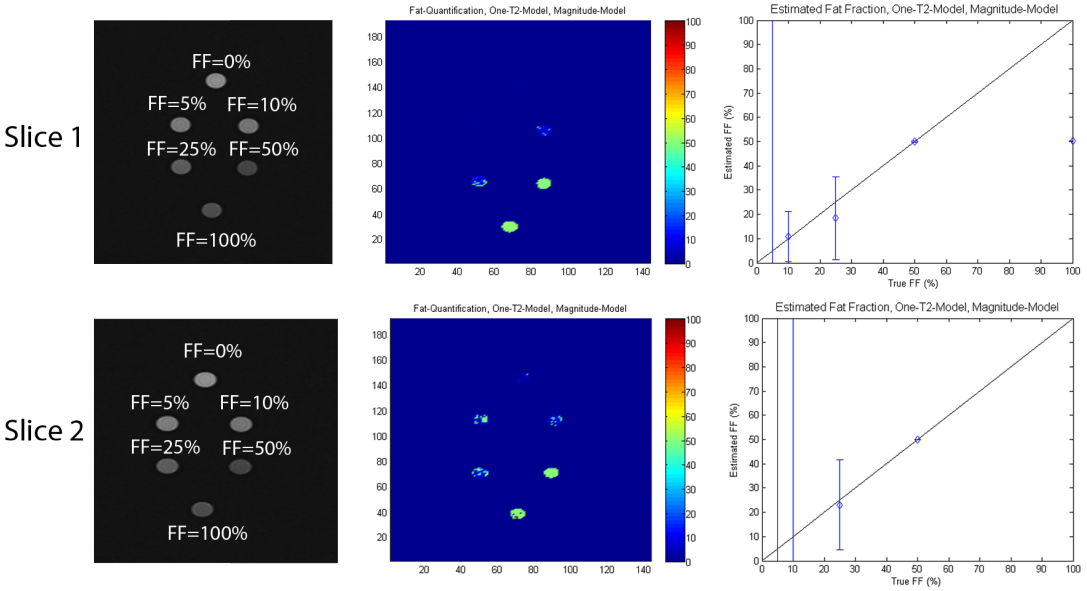


FIGURE 3.14: Phantom FF quantification of images from two different slices using the alternative combination for the magnitude single-decay model.

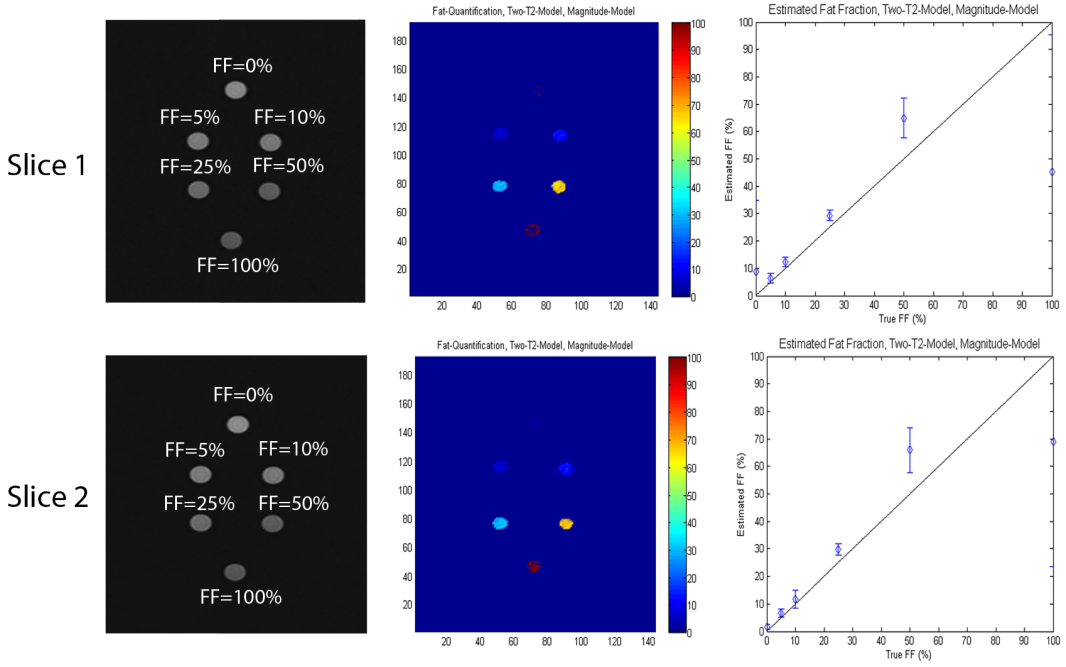


FIGURE 3.15: Phantom FF quantification of images from two different slices using the alternative combination for the magnitude dual-decay model.

Figure 3.14 illustrates that FF estimation is, in general, affected by a large bias. Interestingly, from the comparison with figure 3.12, the precise estimation of the FF in the vial with an emulsion of 50% fat must be stressed.

Results obtained with the alternative TE-ΔTE combination for magnitude dual-decay model is presented in figure 3.15. In contrast with the clinical protocol acquisition, figure 3.15 shows a more robust estimation, particularly for low values of FF. Associated with this quantification, it is noteworthy the low FF errors, in opposition with the magnitude single-decay model.

### 3.2.3 Complex model alternative combinations

Results obtained with alternative TE-ΔTE combinations are expressed in figures 3.16 and 3.17.

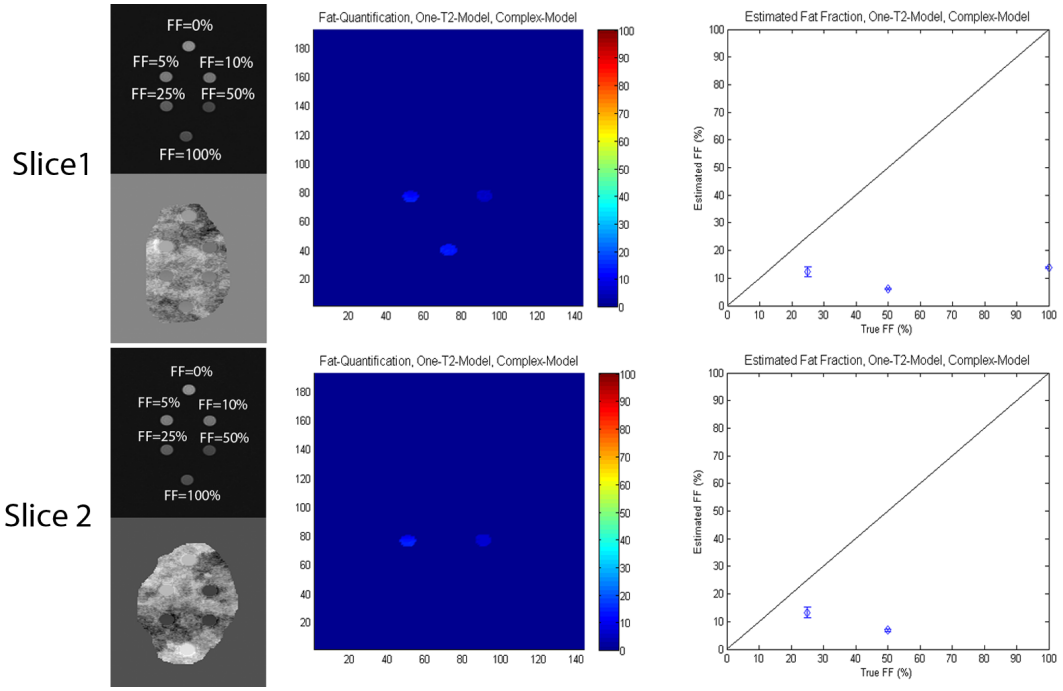


FIGURE 3.16: Phantom FF quantification of images from two different slices acquired using the alternative combination for the complex single-decay model.

Results show a severe disparity from the true amount of FF. Similarly to the clinical protocol, the present quantification shows values mainly below the true values. In addition, the quantification disparity from slice to slice is even larger than in the case of the magnitude models, particularly in the case of dual-decay model.

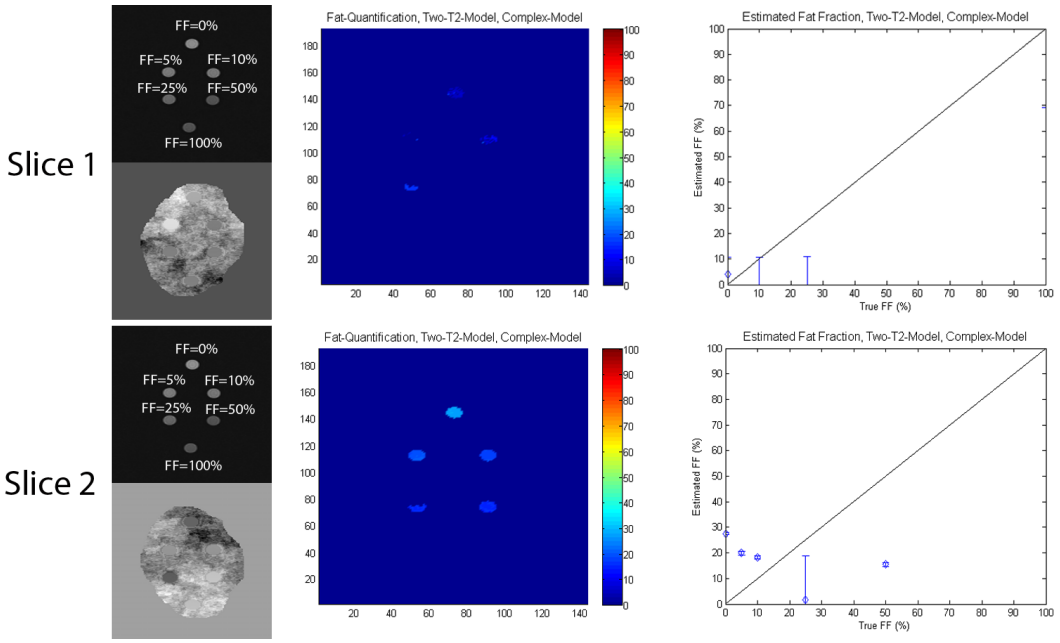


FIGURE 3.17: Phantom FF quantification of images from two different coronal slices acquired using the alternative combination for the complex dual-decay model.

## 3.3 *In-vivo* Studies

Figure 3.18 shows the parametric maps obtained for FF quantification in the liver for 3 controls using the magnitude model with single- and dual-decay constants. Results suggest that the magnitude single-decay model is very accurate to estimate low FF values. In fact, all parametric maps obtained with this model show a liver fat accumulation inferior to 10% (FF threshold for steatosis). On the contrary, magnitude dual-decay model systematically fails to correctly sort out the signal intensity of water and fat. In that sense, voxels where the FF is close 0% are wrongly associated with a FF close to 100%. Similarly, voxels in the subcutaneous fat are wrongly associated with a FF of 0%.

Figure 3.19 shows FF parametric maps of three patients obtained with the magnitude model. As for the controls, here, magnitude single-decay model also performed better in estimating FF values. In additions, magnitude dual-decay model continues to incorrectly overestimate FF values.

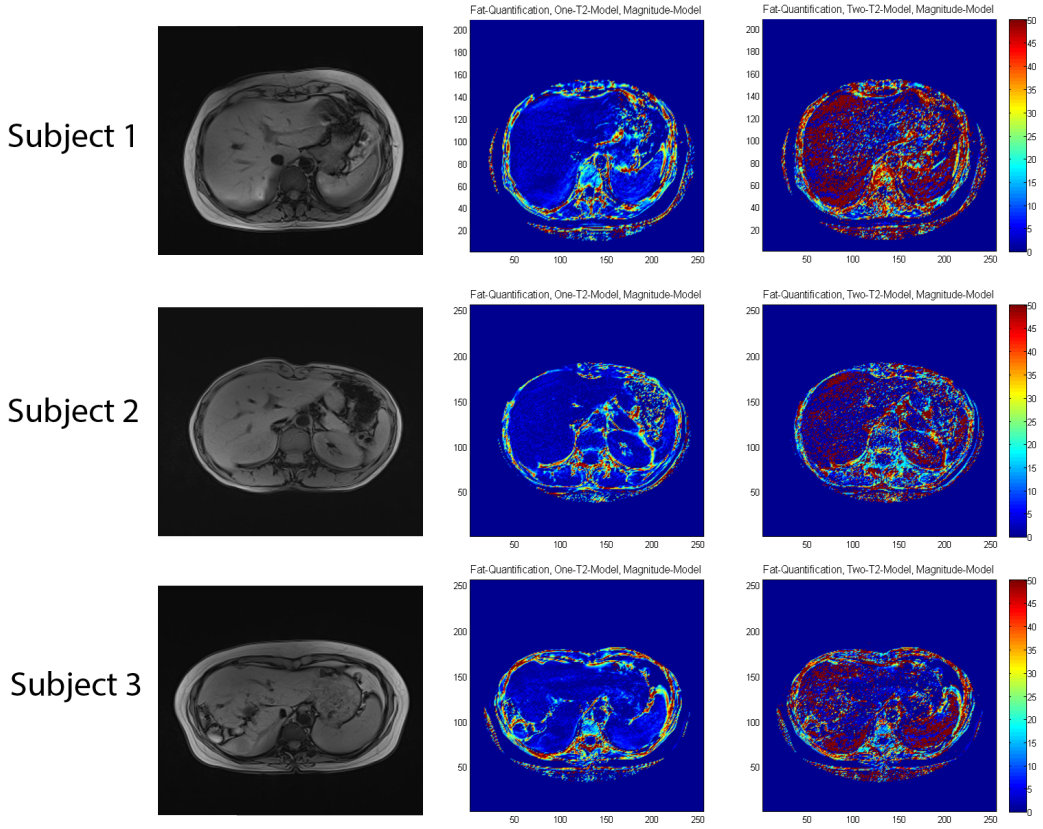


FIGURE 3.18: Parametric maps of liver FF in three control subjects obtained with the magnitude model.

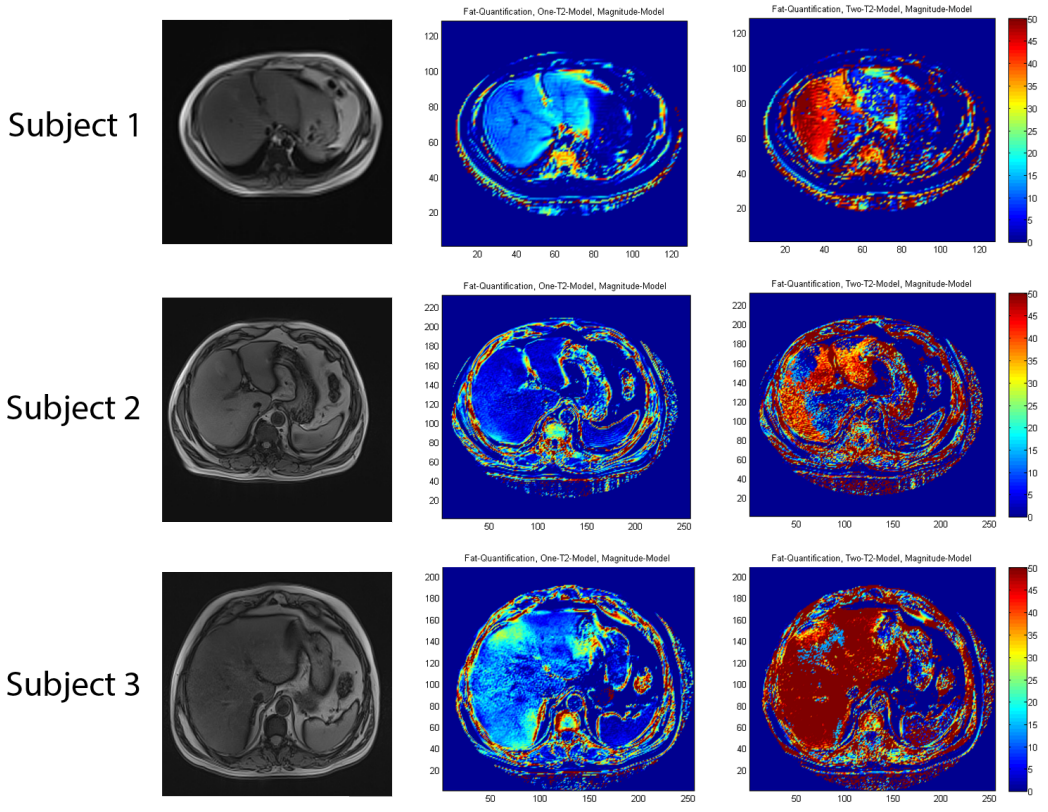


FIGURE 3.19: Parametric maps of liver FF in three patient obtained with the magnitude model.

# Chapter 4

# Discussion

The goal of the present work was to optimize the acquisition strategy for FF quantification in the liver. The approach that was followed consisted in:

1) Study the dependence of FF quantification error and bias on distinct TE-$\Delta$TE combinations both for magnitude and complex models;

2) Find alternative TE-$\Delta$TE combinations for FF quantification and test their robustness experimentally;

3) Compare with the standard clinical protocol.

Simulation results indicate that TE-$\Delta$TE combinations have a strong influence in the FF estimation error. Overall, different TE-$\Delta$TE combinations optimize FF quantification for different conditions. In fact, results show that TE-$\Delta$TE combinations which minimize the errors and biases in one model, not necessarily do the same in other models (e.g. figure 3.3). Moreover, distinct TE-$\Delta$TE combinations minimize different estimation parameters, which implies that there is not a single optimal TE-$\Delta$TE combination to estimate FF with minimum error and bias.

FF estimation with the magnitude model is more sensitive to noise [4, 37], especially when considering dual-decay relaxation constants. In the presence of noise and particularly for low values of FF, this model may lead to an overestimation of the true amount of fat as can be clearly observed in figure 3.4. The sensitivity of the magnitude model to the presence of noise is explained by

the fact that magnitude images amplify the noise that is present in the complex data acquired in the scanner. In fact, the square operation on complex data transforms and amplifies the noise with Gaussian distribution into noise with Rician distribution. In addition, the sensitivity of the magnitude model to noise is also due to the fact that it discards the phase information that is available in the data. As a consequence this model is not able to distinguish the major component in the voxel. This becomes evident in the in *vivo-studies*, where the magnitude dual-decay model systematically estimates high FF in controls known to have a low FF. Another consequence of the lack of phase information is that the estimations for FF near 50% are strongly dependent on the TE-$\Delta$TE combination that is used to sample the signal. This is explicitly demonstrated in the bias colour maps (figures 3.4 and 3.6) where an intricate pattern of higher and lower biases is observed. In contrast, complex model exhibits a more robust fitting, achieving higher values of NSA and lower errors, especially for dual-decay constants. For both magnitude and complex models, results demonstrate that as the values of FF increase, more TE-$\Delta$TE combinations, where FF error and bias are minimized appear. This is the result of the increased signal intensity from fat protons as FF values increase.

The way relaxations effects are included in the model influence the FF estimation [4, 7]. Magnitude model profits from considering a single-decay constant for water and fat, whereas complex model appears to perform better considering two different relaxation constants. The justification for this lies in the fact that the complex model with dual-decay constants is a more realistic description of the data than any other model. This is proved by the low FF bias and errors that are obtained, especially for higher values of FF.

The studies regarding magnetic field inhomogeneities indicate that complex model leads to a highly biased FF estimations for off-resonance frequencies. This is enhanced in figure 3.7 in which, even for optimized TE-$\Delta$TE combinations, minimization is only achieved for frequencies very close to the resonance frequency. Simulation results shows that, in the presence of the cumulative effects of phase errors and noise, the complex model may show difficulties performing fat quantification.

Finally, simulation results demonstrated that the clinical protocol is not optimized for FF quantification. Generally, the clinical TE-$\Delta$TE combination falls on regions of larger errors, which may lead to incorrect estimations.

In the development of a new strategy for image acquisition, several considerations were made in order to properly identify alternative TE-ΔTE combinations from the simulation studies. Finding the best TE-ΔTE combination that simultaneously minimizes the bias and errors associated with all the parameters ($T^*_{2water}$, $T^*_{2fat}$, and FF), is difficult. The problem here is that a TE-ΔTE combination which optimizes a parameter may also dramatically increase the error and bias in others. Therefore, the choice was to consider TE-ΔTE combinations that would roughly optimize the error and bias in FF, while keeping $TE_{min}$ and TE-ΔTE as small as possible in order to maximize image SNR. Finally, there were hardware limitations: the whole-body MRI scanner does not allow first TEs and ΔTEs lower than 2.40ms and 1.26ms, respectively.

Phantoms experiments emphasise the limitations of the clinical protocol to correctly estimate certain amounts of fat. Although magnitude single-decay model shows accurate estimates for certain values of FF (0%, 5% and 100%) it also shows weak estimations for FFs between 5% and 100%. The better quantification of low FF values in phantoms using the clinical protocol contradicts the simulation results. In phantom experiments, differences in FF estimations for different coronal slices are observed. This suggests that although, the emulsions appears to be homogeneous at a macroscopic scale, that is probably not so at a microscopic level. Furthermore, as the amount of FF increases more inhomogeneities may be present in the emulsions, which can reduce sampling quality leading to more incorrect estimations. The magnitude dual-decay model also shows an inaccurate quantification of fat, with the majority of the estimates lying below the true value of FF.

When the FF is estimated using the alternative TE-ΔTE combinations, improvements are found in the magnitude model. It is noteworthy the precise estimation of FF of 50% using magnitude single-decay model where the FF error is almost zero. This observation is in support of our simulation data and emerges as results of our optimization process (table 3.2). Magnitude dual-decay model also expresses enhanced performance in low FF range, being capable of estimating FF of 0%, 5%, 10% more accurately, but failing in estimating FF=100%. Nevertheless, we observed that in both models, an unbiased estimation of the FF in a given vial often corresponds to the biased estimation of FF in other vials, which provide further evidence of the difficulties in choosing a single TE-ΔTE combination that minimizes all FF simultaneously.

For the complex model, alternative TE-$\Delta$TE combinations with lower error and bias compared to magnitude model were identified. Nevertheless, even for these alternative TE-$\Delta$TE combinations, the complex model often fails the FF estimation, which implies that the drawbacks associated with the complex model such as the presence of phase errors may be determinant in practice.

*In-vivo* experiments, using the clinical protocol and the magnitude single-decay model show that it can correctly identify subjects with small amounts of liver fat as opposed to patients with steatosis. However, it also shows how it fails to correctly estimate the FF in subcutaneous fat. This implies that its use in situations where image SNR is lower may originate problems in FF quantification.

This work presents some limitations. In the first place, the fact that the emulsions of our phantom may not be totally homogeneous is a confounding effect in the interpretation of these results. However, obtaining homogeneous emulsions of water and fat is extremely difficult. For instance, the preparation of a macroscopically homogeneous emulsion with FF=75% was not possible. This work also leads to several important conclusions. It is demonstrated that new acquisition protocols can be developed to improve FF quantification. This is particularly important for magnitude model, which is commonly used in clinical procedures. It is also demonstrated that an optimal model or TE-$\Delta$TE combinations to perform FF quantification does not exist, but rather better options for different situations. Therefore, when developing a complete acquisition protocol for FF quantification, a compromise between distinct TE-$\Delta$TE combinations, different models and the expected range of FFs will have to be taken into account. Finally, the complex model with dual-decay constants together with the appropriate changes in the pulse sequence in order to minimize the effects of phase errors, may emerge as the best solution to improve FF quantification

# Chapter 5

# Conclusion

In the present work the problem of liver fat quantification using chemical shift imaging, was investigated with a view at data acquisition optimization at 3T. The effects of noise, phase errors, relaxation effects and especially the influence of distinct TE-$\Delta$TE combinations, so far largely overlooked in the literature, in FF estimation, were evaluated for four distinct models.

In our approach, we demonstrated, theoretically, that good FF estimations can be obtained, suggesting that enhanced fat quantification can be performed by means of correctly choosing the TE-$\Delta$TE combinations. Moreover, it was shown that better FF estimations are obtained for the complex model that is potentially more precise in determining the FF because it describes the data with more completeness. However, the potential advantages of the complex model are largely overshadowed by the inaccuracies that are introduced by phase errors, in the presence of magnetic field inhomogeneities. Since the latter are more prominent at high field strength (3T and above), attention should be given to pulse sequence optimization to minimize phase errors.

We also demonstrate that the problem of FF estimation from ME-GRE images is not a straightforward procedure and involves several complexities, at both image acquisition and image post-processing levels. The standard clinical protocol, based on the magnitude model, has several flaws and needs improvement. Nevertheless, we demonstrate that the standard clinical can be used as way to perform early steatosis staging: which may allow us to constrain ranges

of FFs. This fact in association with new enhanced FF quantification protocols, can emerge as a possible way to develop a complete new strategy for fat quantification using chemical shift imaging.

## 5.1 Future Work

The development of a complete user interface for the application that was developed to quantify liver FF on voxel-by-voxel basis is the next step to extend FF quantification to clinical routine. Finally, the acquisition of in vivo phase images is of great importance to address the performance of the complex model in-vivo. Furthermore, pulse sequence optimization will be carried-out in order to minimize the effects of phase errors on FF quantification using the complex model.

# Bibliography


[1] Neuschwander-Tetri and Caldwell. Nonalcoholic steatohepatitis: Summary of an aasld single topic conference. *Hepatology*, 37(5):1202–1219, 2003.

[2] M. Hall Pauline and Kirsh Richard. Pathology of hepatic steatosis, nash and related conditions. In *Fatty Liver Disease, NASH and Related Disorders*. Blackwell, 2005.

[3] Niederau Claus. *Hepatology, a clinical textbook*, chapter NAFLD and NASH. Flying Publisher, 2013.

[4] Hernando D, Liang Zhi-Pei, and Kellman P. Chemical shiftbased water/fat separation: A comparison of signal models. *Magn Reson Med*, 64:811–822, 2010.

[5] Gui B, Petit J, and Loffroy R. Quantification of liver fat content: Comparison of triple-echo chemical shift gradient-echo imaging and in vivo proton mr spectroscopy. *Radiology*, 250:95–102, 2009.

[6] Gui B, Petit J, and Loffroy R. Mapping of liver fat with triple-echo gradient echo imaging: validation against 3.0T proton mr spectroscopy. *Mag Reson*, 19:1786–1793, 2009.

[7] Chebrolu V, Hines C, Yu H, Pineda A, Shimakawa A, Mckenzie C, Samsonov A, Brittain J, and Reeder S. Independent estimation of T2* for water and fat for improved accuracy of fat quantification. *Mag Reson Med*, 63: 849–857, 2010.

[8] Arias Irwin M et. al. *The Liver, biology and pathobiology*. Wiley-Blackwell, fifth edition, 2009.

[9] Netter Frank H. *Atlas of Human Anotomy*. Saunders, fifth edition, 2010.

[10] Gines Peres and Kamath Patrick S. *Chronic Liver Filure, mechanisms and management*. Humana Press, 2011.

[11] Highleyman L and Fransiscus A. An introduction to the liver. www.hcadvocate.org, 2012.

[12] Farrell Geofrey C et al. An itroduction to nash and related fatty liver disordrs. In *Fatty Liver Disease, NASH and Related Disorders*. Blackwell, 2005.

[13] Maheshwari and Thuluvath. Cryptogenic cirrhosis and nafld. *The American journal of gastroenterology*, 101:664–668, 2006.

[14] LaBrecque Douglas et. at. Nonalcoholic fatty liver disease and nonalcoholic steatohepatitis. Technical report, World Gastroenterology Organization, 2012.

[15] McCoullough AJ. The epidemiology and risk factors of nash. In *Fatty Liver Disease, NASH and Related Disorders*. Blackwell, 2005.

[16] Angulo P. Nonalcoholic fatty liver disease. *N Engl J Med*, 334:1221–1231, 2002.

[17] Wieckowska A, McCullough AJ, and Feldstein AE. Noninvasive diagnosis and monitoring of non-alcoholic steatohepatitis: present and future. *Hepatology*, 46:582–589, 2007.

[18] Saas D, Chang P, and Chopra Kapil B. Nonalcoholic fatty liver disease: a clinical overview. *Digestive Diseases and Science*, 50:171–180, 2005.

[19] Gastaldelli A, Cusi K, and Pettiti M. Relationship between hepatic/visceral fat and hepatic insulin resistance in nondiabetic and type 2 diabetic subjects. *Gastroenterology*, 133:496–506, 2007.

[20] Falck-Ytter Y, Younossi ZM, Marchesini G, and McCullough AJ. Clinical features and natural history of nonalcoholic steatosis syndromes. *Semin Liver Dis*, 21:17–26, 2001.

[21] Bravo A, Sheth S, and Chopra S. Liver biopsy. *N Engl J Med*, 334:495–500, 2001.

[22] Haacke Mark, Brown Robert, Thompson Michael, and Venkatesan Ramesh. *Magnetic Resonance Imaging, physical principles and sequence design*. Wiley-Liss, 1999.

[23] Brown Mark and Semelka Richard. *MRI, basic principles and aplications*. Wiley-Liss, third edition, 2003.

[24] Westbrook Catherine and Kaut Carolyn. *MRI in pratice*. Blackwell, second edition, 1998.

[25] Smith Nadine B and Webb Andrew. *Introduction to Medical Imaging*. Cambridge university press, 2011.

[26] Dixon WT. Simple proton spectroscopic imaging. *Radiology*, 154:189–194, 1984.

[27] Bydder M, Yokoo T, Hamilton G, Middleton MS, Chavez AD, Schwimmer JB, Lavine JE, and Sirlin CB. Relaxation effects in the quantification of fat using gradient echo imaging. *Magn Reson Im*, 26:347–359, 2008.

[28] ORegan DP, Callaghan MF, Wylezinska-Arridge M, Fitzpatrick J, Naoumova RP, Hajnal JV, and Schmitz SA. Liver fat content and T2*: simultaneous measurement by using breath-hold multiecho mr imaging at 3.0T: feasibility. *Radiology*, 247:550–557, 2008.

[29] Yokoo T, Bydder M, Hamilton G, Middleton MS, Gamst AC, Wolfson T, Hassanein T, Patton HM, Lavine JE, Schwimmer JB, and Sirlin CB. Nonalcoholic fatty liver disease: diagnostic and fat-grading accuracy of low-flip-angle multiecho gradient-recalled-echo mr imaging at 1.5T. *Radiology*, 251:67–76, 2009.

[30] Reeder SB, Hargreaves BA, Yu H, and Brittain JH. Homodyne reconstruction and ideal water-fat decomposition. *Magn Reson Med*, 54:586–593, 2005.

[31] Yokoo T, Bydder M, Hamilton G, Middleton MS, Gamst AC, Wolfson T, Hassanein T, Patton HM, Lavine JE, Schwimmer JB, and Sirlin CB. Estimation of hepatic proton-density fat fraction by using mr imaging at 3.0T. *Radiology*, 258:749–759, 2011.

[32] Hansen K, Schroeder ME, Hamilton G, Sirlin CB, and Bydder M. Robustness of fat quantification using chemical shift imaging. *Mag Reson Im*, 30: 151–157, 2012.

[33] Heredia V, Ramalho M, Campos R, Dale B, and Semelka C. Liver-vessel cancellation artifact on in-phase and out-of-phase mri imaging: A sign of ultra-high liver fat content. *J Mag Reson Im*, 35:1112–1118, 2012.

[34] Hernando D, Hines CDG, Yu H, and Reeder SB. Addressing phase errors in fat-water imaging using a mixed magnitude/complex fitting method. *Mag Reson Med*, 67:638–644, 2012.

[35] Yu Huanzhou, McKenzie CA, Vu A Shimakawa, and Brau A. Multiecho reconstruction for simultaneous water-fat decomposition and T2* estimation. *J Mag Reson Im*, 26:1153–1161, 2007.

[36] Lee SS, Lee Y, Kim N, Kim SW, and Byun JH. Hepatic fat quantification using chemical shift mr imaging and mr spectroscopy in the presence of hepatic iron deposition: Validation in phantoms and in patients with chronic liver disease. *J Mag Reson Im*, 33:1390–1398, 2011.

[37] Yu Huanzhou, McKenzie CA, Shimakawa, Hamilton G, Sirlin CB, Brittain JH, and Reeder SB. Combination of complex-based and magnitude-based multiecho water-fat separation for accurate quantification of fat-fraction. *J Mag Reson Im*, 66:199–205, 2011.

[38] Yu Huanzhou, McKenzie CA, Shimakawa, Brodsky E, Brittain JH, and Reeder SB. Multiecho water-fat separation and simultaneous R2* estimation with multifrequency fat spectrum modeling. *Mag Reson Med*, 60: 1122–1134, 2008.

[39] Ma J, Wehrli FW, Song HK, and Hwang SN. A single-scan imaging technique for measurement of the relative concentrations of fat and water protons and their transverse relaxation times. *J Mag Reson*, 125:92–101, 1997.

[40] Ma J. Dixon techniques for water and fat imaging. *J Mag Reson Im*, 28: 543–558, 2008.

[41] Hernando D, Haldar JP, Sutton BP, Ma J, Kellman P, and Liang ZP. Joint estimation of water/fat images and field inhomogeneity map. *Mag Reson Med*, 59:571–580, 2008.

[42] Glover GH. Multipoint dixon technique for water and fat proton and susceptibility imaging. *J Mag Reson Im*, 1:521–530, 1991.

[43] George DK, Goldwurm S, MacDonald GA, Cowley LL, Walker NI, Ward PJ, Jazwinska EC, and Powell LW. Increased hepatic iron concentration in nonalcoholic steatohepatitis is associated with increased fibrosis. *Gastroenterology*, 114:311–318, 1998.

[44] Moirand R, Mortaji AM, Loreal O, Paillard F, Brissot P, and Deugnier Y. A new syndrome of liver iron overload with normal transferrin saturation. *Lancet*, 349:95–97, 1997.

[45] Hines C, Yu H, shimakawa A, McKenzie C, Brittain J, and Reeder B. T1 independent, T2* corrected mri with accurate spectral modeling for quantification of fat: Validation in a fat-water-SPIO phantom. *J Mag Reson Im*, 30:1215–1222, 2009.

[46] Parlato M, Dzyubak B, Helfenberger J, and Balge N. Mri phantom for fat quantification. Technical report, BME 400, 2009.

[47] Kokatnur MG, Oalmann MC, Johnson, Malcom GT, and Strong JP. Fatty acid composition of human adipose tissue from two anatomical sites in a biracial community. *Am J Clin Nutr*, 32:2198–2205, 1979.

[48] Belechinger. Tissue-micking gelatin-agar for use in magnetic resonance imaging phantoms. *Medical Physics*, 15:629–636, 1988.

[49] Porath, Olof J, and Janson J. Stabilized agar and method for its stabilization. US Patent 3959251, 1976.

[50] Inc The Lab Depot. Magnetic stirrer, hot plate stirrer. http://www.labdepotinc.com/c-101-lab-stirrer.php.

[51] Data Format Working group. Nifti: Neuroimaging informatics technology initiative. nifti.nimh.nih.gov.

[52] dcm2nii dicom to nifti conversion. mccauslandercenter.sc.edu.

[53] Analysis Group, FMRIB, Oxford, and UK. Fsl. fsl.fmrib.ox.ac.uk.